JGR Solid Earth

RESEARCH ARTICLE
10.1029/2020JB019629

Evolution of Microstructural Properties in Sheared Iron-Rich Olivine

Chao Qi[1], **Yong-Hong Zhao**[2], **Mark E. Zimmerman**[3], **Daeyeong Kim**[4], and **David L. Kohlstedt**[3]

[1]Key Laboratory of Earth and Planetary Physics, Institute of Geology and Geophysics, Chinese Academy of Sciences, Beijing, China, [2]Department of Geophysics, Peking University, Beijing, China, [3]Department of Earth & Environmental Sciences, University of Minnesota, Minneapolis, MN, USA, [4]Division of Polar Earth-System Sciences, Korea Polar Research Institute, Incheon, South Korea

Key Points:

- The weakest slip system does not change with Fe content, such that CPO development is similar for Fe-rich and Fe-poor olivine
- Seismic anisotropy due to the formation of CPOs in natural olivine aggregates can be modeled using CPOs obtained from iron-rich olivine
- Recrystallized grain size at a given normalized stress increases with increasing Fe content

Supporting Information:

- Supporting Information S1

Correspondence to:
Y. Zhao,
zhaoyh@pku.edu.cn

Citation:
Qi, C., Zhao, Y.-H., Zimmerman, M. E., Kim, D., & Kohlstedt, D. L. (2021). Evolution of microstructural properties in sheared iron-rich olivine. *Journal of Geophysical Research: Solid Earth*, *126*, e2020JB019629. https://doi.org/10.1029/2020JB019629

Received 20 FEB 2020
Accepted 15 JAN 2021

Abstract

Iron-rich olivine is mechanically weaker than olivine of mantle composition, ca. Fo_{90}, and thus is more amenable to study under a wide range of laboratory conditions. To investigate the effects of iron content on deformation-produced crystallographic preferred orientation (CPO) and grain size, we analyzed the microstructures of olivine samples with compositions of Fo_{70}, Fo_{50}, and Fo_{0} that were deformed in torsion under either anhydrous or hydrous conditions at 300 MPa. Electron backscatter diffraction (EBSD) observations reveal a transition in CPO from D-type fabric, induced by dislocation glide on both the (010)[100] and the (001)[100] slip systems, at low strains, to A-type fabric, caused by dislocation glide on the (010)[100] slip system, at high strains for all of our samples, independent of iron content and hydrous/anhydrous conditions. A similar evolution of fabric with increasing strain is also reported to occur for Fo_{90}. Radial seismic anisotropy increases with increasing strain, reaching a maximum value of ∼1.15 at a shear strain of ∼3.5 for each sample, demonstrating that the seismic anisotropy of naturally deformed olivine-rich rocks can be well approximated by that of iron-rich olivine. Based on EBSD observations, we derived a piezometer for which recrystallized grain size decreases inversely with stress to the ∼1.2 power. Also, recrystallized grain size increases with increasing iron content. Our experimental results contribute to understanding the microstructural evolution in the mantle of not only Earth but also Mars, where the iron content in olivine is higher.

1. Introduction

The rheological properties of olivine influence many geological processes on Earth and other planets in our solar system. Experimental studies demonstrate that the rheological behavior of olivine not only depends on thermomechanical parameters, such as stress, temperature (e.g., Carter & Ave'Lallemant, 1970; Chopra & Paterson, 1981), confining pressure (e.g., Borch & Green, 1989; Karato & Jung, 2003; Karato & Rubie, 1997), oxygen fugacity (e.g., Bai et al., 1991; Ricoult & Kohlstedt, 1985), melt content (e.g., Cooper & Kohlstedt, 1986; Hirth & Kohlstedt, 1995a, 1995b; Mei et al., 2002; Scott & Kohlstedt, 2006; Zimmerman & Kohlstedt, 2004) and water content (e.g., Karato et al., 1986; Mackwell et al., 1985; Mei & Kohlstedt, 2000a, 2000b; Tielke et al., 2017), but also on microstructural properties, such as the crystallographic preferred orientation (CPO) (e.g., Hansen et al., 2012a, 2012b) and grain size (e.g., Hansen et al., 2011; Hirth & Kohlstedt, 1995b; Karato et al., 1986). As an olivine single crystal exhibits strong viscous anisotropy (Bai et al., 1991; Durham & Goetze, 1977), the formation of a CPO in an olivine aggregate enhances plastic deformation in one crystallographic direction relative to the others (Hansen et al., 2012b, 2016). Thus, understanding the development of CPOs at different stresses, pressures and chemical conditions helps constrain microstructurally induced weakening/strengthening during deformation and is essential for the application of laboratory-derived flow laws to natural environments (Kohlstedt & Hansen, 2015). During plastic deformation, changes in grain size occur due to dynamic recrystallization and grain growth (Poirier, 1985, pp. 170–190). Experimental studies have determined the relationship between grain size and stress, that is, the grain-size piezometer, which is frequently used for estimating paleostresses in naturally deformed rocks (e.g., Kang & Jung, 2019; Kohlstedt & Weathers, 1980; Mercier et al., 1977; Park & Jung, 2017; Platt & Behr, 2011; Stipp & Tullis, 2003; Tokle et al., 2019; Warren & Hirth, 2006). As grain size plays an important role in flow laws for grain-size sensitive deformation mechanisms, such as diffusion creep and grain boundary sliding accommodated by dislocation creep (disGBS), understanding the evolution of grain size during deformation is critical for interpreting the deformation history of naturally deformed rocks (de Bresser et al., 2001).

Olivine exists as a solid solution, from pure Mg olivine, forsterite (Fo), to pure Fe olivine, fayalite (Fa). In the mantle of Earth, the composition of olivine ranges from Fo_{87} (100 times the molar Fo/(Fo + Fa) ratio) to Fo_{96} with an average of ~Fo_{90} (Deer et al., 1966, pp. 12). In the mantle of Mars, olivine is richer in iron with an estimated composition between Fo_{75} and Fo_{77} (Bertka & Fei, 1997; Morgan & Anders, 1979). In gabbroic intrusions on Earth, olivine is significantly richer in iron with a Fo content of Fo_{69} or smaller (Morse, 1979). In previous studies, the rheological behavior of iron-rich olivine has been investigated systematically with laboratory experiments, yielding flow laws that incorporate the dependence of strain rate not only on temperature and stress but also on iron content (Tasaka et al., 2015; Zhao et al., 2009, 2018). Although Fo_{50} has sometimes been used to study the CPO development of Fe-Mg olivines (Hansen et al., 2012a, 2014, 2016; Tasaka et al., 2016), the influence of iron content on the evolution of microstructures is explored here over a wide range of iron contents in an attempt to provide a unified description that accounts for the influence of iron as well as temperature, stress, and strain.

In this contribution, we performed torsional deformation experiments on samples that cover a range of iron content under both anhydrous and hydrous conditions. By mapping a full radial section of each sample, CPOs and grain sizes at different radii (i.e., different strains and stresses) were determined. The objective of this paper is to investigate the effect of iron content on the evolution of CPO and grain size, in order to provide further insights into the coupling between deformation and microstructure.

2. Methods

2.1. Sample Preparation and Deformation Assembly

Samples for torsion experiments were sliced from deformed samples reported in Zhao et al. (2009) and (2018). Here we briefly describe the preparation procedures. Fayalite, Fo_0 (Fa_{100}), powders were synthesized in a one-atmosphere furnace from powders of Fe_2O_3 and SiO_2 in a molar ratio of 1:1.002 at temperatures close to the melting point of fayalite under a controlled oxygen buffer (Zhao et al., 2009). Powders of Fo_{70} and Fo_{50} were fabricated from mixtures of natural San Carlos olivine, Fo_{90}, and synthetic fayalite. The mixed powders were ground to a particle size of <10 μm and annealed at 1670 K in a one-atmosphere furnace for 16 h under a controlled oxygen buffer. To keep the powders anhydrous, powders were stored in a vacuum oven after the anneal until being cold-pressed. Anhydrous samples of Fo_{70}, Fo_{50} and Fo_0 as well as hydrous samples of Fo_{70} and Fo_{50} were then fabricated by first cold-pressing powders into nickel (Fo_{70} and Fo_{50}) or iron (Fo_0) capsules and then hot-pressing the assemblies. During the cold-press of hydrous samples, two drops of water (~0.03 mL per drop) were added in each capsule. Details of hot-pressing and the axial deformation experiments can be found in Zhao et al. (2009) for anhydrous conditions and Zhao et al. (2018) for hydrous conditions.

The recovered samples were cut into cylinders with a diameter of $2R \approx 9.4$ mm and a thickness of 4.5–5.5 mm. Anhydrous samples were taken from samples PI1050 (Fo_{70}), PI1040 (Fo_{50}), and PI1189 (Fo_0) reported in Zhao et al. (2009). Hydrous samples were taken from samples PI1141 (Fo_{70}) and PI1065 (Fo_{50}) reported in Zhao et al. (2018). Grain sizes and CPOs of samples before torsion deformation are presented in Table 1 and Figure 2, respectively. Although all of the samples have experienced some axial shortening (4.9%–16.9%), the crystallographic axes are oriented roughly randomly, with very weak clustering of crystallographic axes in the Fo_0 sample. The axial strains accumulated in these samples before torsion deformation are presented in Table 1. Cylinders of Fo_{70} and Fo_{50} were then placed into nickel capsules, while cylinders of Fo_0 were inserted into iron capsules, all with porous alumina spacers as end caps, as illustrated in Figure 1a. The rest of the deformation assembly was prepared as detailed in Qi et al. (2015).

2.2. Deformation Experiments

Torsion experiments were performed in a gas-medium apparatus fitted with a torsion actuator (Paterson & Olgaard, 2000). Samples of Fo_{70} and Fo_{50} were deformed at a temperature of $T = 1473$ K ($0.79T_m$ for Fo_{70} and $0.86T_m$ for Fo_{50}) and a confining pressure of $P = 300$ MPa. To ensure water saturation in the samples during

Table 1
Summary of Experiments and Experimental Conditions

Composition	Sample #	Hydrous/ Anhydrous	d_0 (μm)	$\varepsilon_{ax}{}^a$	T (K)	$T/T_m{}^b$	P (MPa)	R (mm)	$\gamma(R)^c$	$\tau(R)^d$ (MPa)	$\dot{\gamma}(R)$ (s^{-1})
Fo_{70}/Fa_{30}	PT263	Anhydrous	33	0.049	1473	0.79	300	4.6	4.4	91	2.6×10^{-4}
	PT278	Hydrous	40	0.107	1473	0.79	300	4.7	4.0	83	4.7×10^{-4}
Fo_{50}/Fa_{50}	PT248	Anhydrous	42	0.169	1473	0.86	300	4.7	4.0	88	2.8×10^{-4}
	PT303	Hydrous	47	0.119	1473	0.86	300	4.6	3.9	65	2.3×10^{-4}
Fo_0/Fa_{100}	PT345	Anhydrous	41	0.071	1373	0.93	300	4.6	3.7	43	2.3×10^{-4}

[a] ε_{ax} is the axial strain accumulated in axial compression before torsion experiment.
[b] T/T_m is homologous temperature. T_m is the solidus temperature at 1 atmosphere estimated based on Bowen and Schairer (1935). For Fo_{70}, $T_m \approx 1863$ K. For Fo_{50}, $T_m \approx 1713$ K. For Fo_0, $T_m \approx 1478$ K. The effect of water content on solidus temperatures is not considered.
[c] $\gamma(R)$ is shear strain at the outer radius.
[d] $\tau(R)$ and $\dot{\gamma}(R)$ are the outer-radius shear stress and shear strain rate measured at the end of each experiment.

the experiments under hydrous conditions, 0.05 mL of distilled water was added to each of the porous alumina discs. For experiments carried out under water-saturated, hydrous conditions, the water fugacity $f_{H_2O} \approx 300$ MPa. The Fo_0 sample was deformed at $T = 1373$ K ($0.93T_m$) and $P = 300$ MPa. All samples were deformed at one or more constant strain rates increments to an outer-radius shear strain of $\gamma(R) = 4.1 \pm 0.4$. Due to slip between sample and spacer or the condition of the apparatus, three samples (PT248, PT278, and PT303) were deformed in two or three sequential experimental runs to accumulate the target strain; samples were removed from the deformation apparatus and rejacketed between runs. Each of the three samples was identified by the number of the final run. For samples deformed at multiple strain rates (PT278 and PT303), the stress associated with the final microstructure was averaged from the last strain-rate increment. After achieving the target strain, each sample was cooled at ~2 K/s to 1300 K (1200 K for the Fo_0 sample) under the same torque as imposed at the end of the deformation experiment to preserve the deformation-produced microstructure and then cooled to room temperature with no torque applied.

2.3. Analysis of Mechanical Data

Rotation angle and torque were recorded as a function of time during each experiment to determine shear stress, τ, shear strain, γ, and shear strain rate, $\dot{\gamma}$. To determine τ, corrections to the measured torque were made to account for the strength of the Fe jacket and Ni or Fe canister. τ was then calculated from the corrected torque, M, using the relationship (Paterson & Olgaard, 2000)

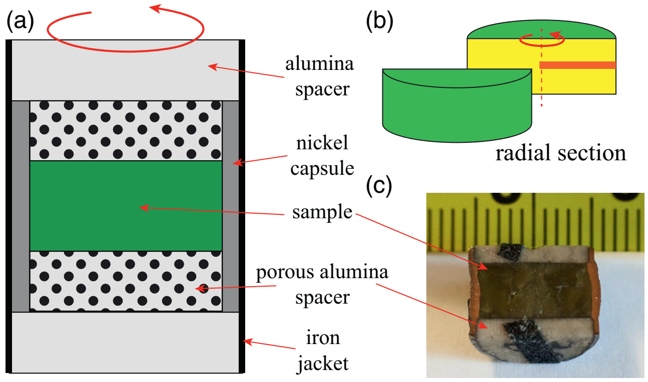

Figure 1. (a) Schematic drawing of the sample assembly for torsion experiments. (b) Drawing of the radial section. The whole radial section (yellow) was mapped with electron-backscatter diffraction(EBSD) at coarse step sizes, while a stripe extending from the axial center to the outer edge (orange) was mapped with EBSD at a fine step size. (c) A photo of the cut and polished radial section of a sample (PT278).

$$\tau = \tau(R) = \frac{\left(3 + \frac{1}{n}\right)M}{2\pi R^3}, \tag{1}$$

where n is the stress exponent in a power-law flow law such as those used later in this paper. The value of n is characteristic of the deformation mechanism. Values of $n = 3.9$ and $n = 3.7$ were used, respectively, for iron-rich olivine deformed by disGBS under anhydrous conditions (Zhao et al., 2009) and by dislocation creep under hydrous conditions (Zhao et al., 2018). The rotation angle θ was converted to shear strain by taking into account the sample dimensions:

$$\gamma = \gamma(R) = \frac{\theta R}{h}, \tag{2}$$

where h is the sample thickness. The rotation angle was also measured from the strain marker on the sample jacket. For all samples except PT248 (Fo_{50} anhydrous), the recorded value of θ corresponded well with the measured value. For PT248, in which slip between sample and spacer

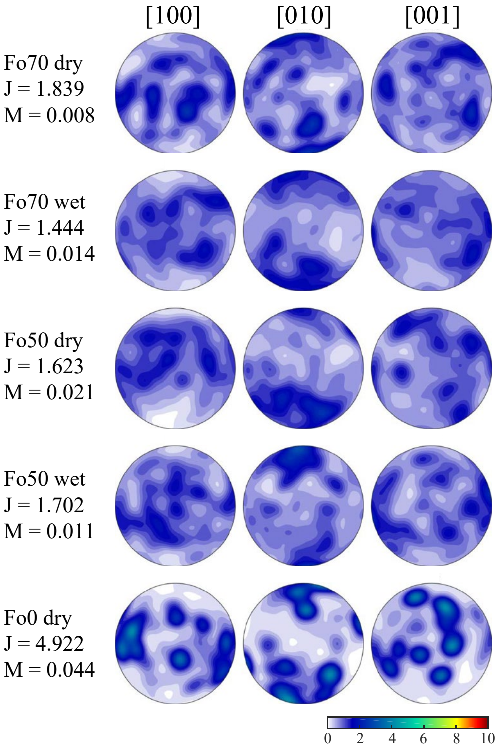

Figure 2. Pole figure illustrating distributions of orientations of [100], [010], and [001] axes. All pole figures are lower-hemisphere projection based on all orientation data of the mapped area. The shortening direction is vertical in the previous triaxial compressive creep experiments reported in Zhao et al. (2009) and (2018). The contours on each stereonet are universally colored by their multiples of uniform distribution (MUD), which is illustrated in the color bar. J- and M-indexes are presented on the left of each group of pole figures.

occurred, the measured value of θ was used to calculate the strain and strain rate. Summary data are presented in Table 1.

To compare with mechanical data from axial compression experiments, the von Mises equivalent stress, σ_{eq}, and the equivalent strain rate, $\dot{\varepsilon}_{eq}$, were calculated from τ and $\dot{\gamma}$ using the relationships

$$\sigma_{eq} = \sqrt{3}\tau \text{ and } \dot{\varepsilon}_{eq} = \frac{\dot{\gamma}}{\sqrt{3}}. \tag{3}$$

Within a torsion sample, shear strain rate increases linearly with increasing radius, r, that is,

$$\dot{\gamma}(r) / \dot{\gamma}(R) = \frac{r}{R}. \tag{4}$$

We applied published flow laws to determine the stress at radius r. Under anhydrous (dry) conditions, our samples deformed by disGBS described by the following flow law (Zhao et al., 2009):

$$\dot{\varepsilon} = \dot{\varepsilon}^0_{gbs} \left(\frac{\sigma}{\mu}\right)^{3.9} \left(\frac{b}{d}\right)^{0.7} \left(\frac{p_{O_2}}{p^{ref}_{O_2}}\right)^{0.2} X_{Fa}^{1.1} \exp\left(-\frac{Q_d + \alpha_d X_{Fa}}{RT}\right). \tag{5}$$

In Equation 5, $\dot{\varepsilon}^0_{gbs} = 5.7 \times 10^{24}$ s^{-1} is a material dependent parameter, μ is the shear modulus, b is the Burgers vector of length 4.75×10^{-4} μm, p_{O_2} is oxygen partial pressure with $p^{ref}_{O_2} = 1$ Pa, $Q_d = 435$ kJ/mol is the activation energy for creep, X_{Fa} is the mole fraction of fayalite, $\alpha_d = -50$ kJ/mol reflects the dependence of activation energy on fayalite content, and R is the gas constant. In the original reporting of this flow law, a grain-size dependence of $(1/d)^2$ was assumed; the dependence used here, $(1/d)^{0.7}$, was determined in subsequent studies (Hansen et al., 2011, 2012a). The dependence of strain rate on p_{O_2} was obtained from the work of Keefner et al. (2011). Also, in the original reporting of this flow law, μ and b were not included in the non-linear least-squares fit of the data even though they were reported in the flow law to non-dimensionalize the stress and grain size terms. The values for the parameters reported here correct these errors. Under hydrous (wet) conditions, our samples deformed by dislocation creep described by the following flow law (Zhao et al., 2018):

$$\dot{\varepsilon} = \dot{\varepsilon}^0_{disl} \left(\frac{\sigma}{\mu}\right)^{3.7} \left(\frac{f_{H_2O}}{f^{ref}_{H_2O}}\right)^{5/4} X_{Fa}^{0.2} \exp\left(-\frac{Q_w + \alpha_w X_{Fa}}{RT}\right). \tag{6}$$

In Equation 6, $\dot{\varepsilon}^0_{disl} = 1.5 \times 10^{20}$ s^{-1}, f_{H_2O} is water fugacity with $f^{ref}_{H_2O} = 1$ MPa, $Q_w = 525$ kJ/mol, and $\alpha_w = -100$ kJ/mol. In the original reporting of this flow law, μ was not included in the non-linear least squares fit of the data, even though it was included in the flow law to non-dimensionalize the stress term. The values for the parameters reported here correct this error.

Note that these two flow laws in Equations 5 and 6 are determined at strains <0.2, and therefore, cannot be directly applied to samples deformed to larger strains. Hansen et al. (2012a) reported that the stress and grain-size exponents in the flow law do not change with increasing strain, and strain weakening can be explained by the combination of grain-size reduction and CPO development. The weakening induced by CPO development can be quantified by a factor describing the degree of geometric softening, F, which is 1 for an isotropic polycrystalline materials and ranges between 1 and 0 depending on the strength of the dominant slip system relative to the isotropic case. Based on Equation 12 in Hansen et al. (2012a), F can be related to strain as

$$F = F_{ss} + (1 - F_{ss})\exp\left(-\frac{\varepsilon}{\varepsilon_c}\right), \tag{7}$$

where the value of F at steady state, F_{ss}, is estimated to be 0.72 for (010)[100] slip system, and the critical strain for CPO development, ε_c, is estimated to be 1 for Fo_{50}. Then the stress at a higher strain, σ_{hs}, can be calculated from the low-strain stress, σ_{ls}, derived from the flow law using the relationship

$$\sigma_{hs} = F \times \sigma_{ls}. \tag{8}$$

Thus, for the samples in our study, we can calculate the stress at a radius, r, from the measured values of strain rate and grain size (see next subsection), based on Equations 5–8.

2.4. Analysis of Microstructure

After each deformation experiment, a radial section through the axial center of the sample was prepared for analyzing the crystallographic orientations; the process is illustrated in Figure 1. The radial section was polished down to a diamond grid size of 0.5 μm, followed by a final step with 40-nm colloidal silica. Analyses of radial sections of samples deformed in torsion allow for obtaining microstructural data at different radii, that is, at different strains, strain rates and stresses. However, some microstructural features, such as tilt walls, cannot be observed, because most of them do not intersect the polished surface.

To obtain crystallographic data, orientation maps with different step sizes were collected for all sections using a scanning electron microscope equipped with an electron-backscatter diffraction (EBSD) system. For EBSD analyses, step sizes of 4–7 μm were used to map the whole radial section, while a finer step size of 1.5 μm was used to map smaller areas on the radial section. Information of the orientation maps are summarized in Table 2. Raw orientation data were processed using HKL CHANNEL5 software, including removal of single mis-indexed points, assigning the average orientation of neighboring pixels to unindexed points, and removal of systematic mis-indexed points, as outlined, for example, in Hansen et al. (2011). Grains were constructed from processed orientation data using the MTEX toolbox (Bachmann et al., 2011). Grain boundaries were drawn where the misorientation between neighboring pixels exceeded 10°. No extrapolation of orientation data was applied in MTEX since the data were already processed by the HKL CHANNEL5 software.

To distinguish recrystallized grains from relict grains, grains were separated based on their degrees of intracrystalline distortion. For each grain, grain orientation spread (GOS) was used as a measurement of intracrystalline distortion. The threshold value of GOS that separates recrystallized and relict grains was determined by the method described in Cross et al. (2017). The threshold value was generally between 2.0 and 2.5°. Grains with values of GOS below the threshold value were considered as recrystallized.

Grain size was determined by applying a scaling factor of $4/\pi$ to the equivalent diameter of a circle with the area of each recrystallized grain in cross section. In the analysis of the average grain size for a map, grains containing less than 4 pixels or lying on the edge of the map were excluded. We calculated both the arithmetic mean and the geometric mean for the average grain size in selected areas.

For easy comparison with previous studies, orientation data were rotated into a kinematic reference frame, that is, the plane containing the shear direction and shear plane normal. Orientation distributions were generated from all data points from at least 500 individual grains with a half-width angle of 10° using the MTEX toolbox in MATLAB (Bachmann et al., 2010; Mainprice et al., 2015). To quantify the strength of the CPOs, both the J-index (Bunge, 1982) and the M-index (Skemer et al., 2005) were used.

To quantify the shape of the distribution of crystallographic axes in pole figures, an eigenvalue analysis following Woodcock (1977) was employed. Normalized eigenvalues, S_1, S_2, and S_3, calculated from the orientation tensor, obey the relationships

$$S_1 + S_2 + S_3 = 1 \tag{9}$$

Table 2
Summary of Results From EBSD Analyses

Sample #	Data for CPO			Data for microstructure		
	Step size (μm)	# Indexed	# Grains	Step size (μm)	# Indexed	# Grains
PT248	7	629309	60316	1.5	617338	8191
PT263	5	1226602	176934	1.5	597728	16366
PT278	8	721695	92970	1.5	590263	8266
PT303	8	524532	31925	1.5	5083240	18916
PT345	4	1758097	40764	1.5	5273959	19026

EBSD, electron-backscatter diffraction; CPO, crystallographic preferred orientation.

and

$$S_1 \geq S_2 \geq S_3. \tag{10}$$

The shape factor of the distribution of axes, K, is then defined by

$$K = \frac{\ln(S_1 / S_2)}{\ln(S_2 / S_3)}. \tag{11}$$

For the orientations of a specific group of crystallographic axes, $K > 1$ indicates that the distribution of axes forms a cluster, and $K < 1$ indicates that the distribution of axes forms a girdle.

2.5. Calculation of Seismic Properties

To calculate the seismic anisotropy of an aggregate, stiffness tensors for individual grains obtained at room pressure and temperature for olivine (Abramson et al., 1997) were averaged based on the measured distribution of crystallographic orientations using the MTEX toolbox for MATLAB (Mainprice et al., 2011). The Hill average was used, as it yields the best approximation of the magnitudes of individual elastic constants (Zhong et al., 2014). Magnitudes of seismic anisotropy were then calculated using the average stiffness tensor, following the procedures described by Hansen et al. (2014) and Skemer and Hansen (2016). In Voigt notation, the stiffness tensor is described by the 36 components in C_{ij}, where i and j range from 1 to 6 (e.g., Karato, 2008, pp. 53). In our reference frame, subscripts 1, 2, and 3 correspond to the shear direction, the normal to the shear plane, and the vorticity direction, respectively. We calculated the radial anisotropy, $(V_{\mathrm{SH}}/V_{\mathrm{SV}})^2$, assuming the shear plane is horizontal. V_{SH} and V_{SV} are the velocities of S-waves polarized parallel to the shear plane and the normal to the shear plane, respectively. The radial anisotropy can be calculated using components of the average stiffness tensor through the relationship (Montagner & Nataf, 1986)

$$\left(\frac{V_{SH}}{V_{SV}}\right)^2 = \frac{\frac{1}{8}(C_{11} + C_{22}) - \frac{1}{4}C_{12} + \frac{1}{2}C_{66}}{\frac{1}{2}(C_{44} + C_{55})}. \tag{12}$$

2.6. FTIR Analysis

Hydroxyl contents of the olivine aggregates were determined from Fourier transform infrared (FTIR) analyses of doubly polished slices ~0.3 mm in thickness and ~5 mm in length and width. FTIR spectra were collected on two deformed hydrous samples. Details of the analysis can be found in Zhao et al. (2018).

3. Results

3.1. Mechanical Data

The environmental conditions along with the outer radius shear strain, shear stress, and shear strain rate at the end of each experiment are summarized in Table 1. Graphs of outer-radius shear stress plotted against outer-radius shear strain (hereafter "stress" and "strain" for brevity in this subsection) are presented in Figure 3. Stresses were calculated using the reported flow laws, as described in Section 2.3. All curves show a rapid rise in stress to a peak stress at a relatively small strain of ~0.3. In experiments PT263 (Fo_{70}, anhydrous, $T = 0.79T_m$), PT278 (Fo_{70}, hydrous, $T = 0.79T_m$) and PT248 (Fo_{50}, anhydrous, $T = 0.86T_m$), the peak stress was followed by a steep drop in stress with increasing strain. In PT263, stress increased rapidly to a second peak after the steep drop, due to an imposed increase in strain rate; after this second peak, stress gradually evolved to a plateau at $\gamma > 3$. In PT278, after the steep drop, stress increased and then decreased with increasing strain due to slip between the sample and a spacer, which led to the end of the first part of this experiment. The sample was then taken out of the deformation apparatus and re-jacketed with new spacers and pistons. In the second part, stress increased in steps that correlate with stepped increases in strain rate. In PT248, the steep drop in stress was due to slip between the sample and one of the spacers, which led to the end of the first part of the experiment. The second part also ended with a rapid decrease in stress. In the third part, stress slowly evolved within a range of ±10 MPa with increasing strain. In PT303 (Fo_{50}, hydrous, $T = 0.86T_m$), stress decreased gradually with increasing strain and plateaued at $\gamma > 2.5$. In PT345 (Fo_0, anhydrous, $T = 0.93T_m$), stress remained roughly constant after the peak stress at $\gamma < 1.5$, gradually dropped at $1.5 < \gamma < 2.5$, and slightly increased at $\gamma > 2.5$. Although strain-rate steps were made in three of the experiments, the mechanical data were not further investigated, as the mechanical behaviors of these samples have been investigated and reported in Zhao et al. (2009),and (2018). Flow laws of iron-rich olivine under anhydrous and hydrous conditions have been determined in previous studies (Tasaka et al., 2015; Zhao et al., 2009, 2018). The mechanical data are compared with the flow laws in Figure S1. Note that the data represent the strain rate at the outer radius and the stress calculated based on the torque over the full radius, such that, the data points should only be compared qualitatively to the flow laws.

3.2. FTIR Results

The FTIR spectra in Figure 4 obtained from two hydrous samples, Fo_{70} (PT278) and Fo_{50} (PT303), after deformation demonstrate that these samples were indeed sheared under hydrous conditions. The broadband extending from 3,000 to 3,700 cm^{-1} arises from water trapped in pores. Note that this approach yields the "free water" not the structurally bound water/hydroxyl (OH). This source of water insures that deformation of these two samples occurred under water-saturated conditions (Karato et al., 1986). The observations for hydrous samples are in good agreement with those reported by Zhao et al. (2018) for samples of Fe-rich olivine deformed in triaxial compression and with those reported by Tasaka et al. (2016) for samples of Fe-rich olivine deformed in torsion. Likewise, the OH concentration in samples deformed under anhydrous conditions was below the FTIR detection limit (Zhao et al., 2018).

3.3. Crystallographic Preferred Orientations

In this subsection, CPOs of samples with different iron contents deformed under either anhydrous or hydrous conditions are described. The results are presented as orientation maps for radial sections, plots of CPO strength versus radius, and distributions of orientations at different radii in Figures 5–7.

3.3.1. Strain series

In all samples, near the axial center, $r = 0$, the crystallographic axes are randomly distributed. With increasing radius, that is, with increasing strain, the crystallographic axes gradually concentrate into clusters. The strength of the CPO, characterized by the J- and M-indexes, increases roughly linearly with increasing radius. Converting radius to shear strain and averaging the indexes from regions at the same strain (symmetric with respect to the torsional axis), plots of fabric strength versus local shear strain, as illustrated in Figure 8a, reveal that M-index increases roughly linearly with increasing strain for $\gamma < 3.5$ and then remains constant or decreases slightly for $\gamma > 3.5$.

For regions at $r \geq 1$ mm in all samples, a weak secondary cluster of [100] axes occurs 60–70° to the primary [100]-axes cluster, synthetic to the shear direction; the only exception is the region at $r = 4.2$ mm in the hydrous Fo_{50} sample (PT303). With increasing radius (strain), the primary [100]-axis cluster strengthens and the secondary [100]-axis cluster weakens, as characterized by their values of multiples of uniform distribution (MUD). At small radii, [010] and [001] axes form girdles subnormal to the shear direction. With increasing radius, [010] and [001] axes become less girdled and gradually concentrate into elongated clusters. The strengths of the [010]- and [001]-axis clusters also increase with increasing radius (strain), as characterized by the values of MUD. Near the outer radius of all samples, CPOs are characterized by a strong primary cluster of [100] axes aligning parallel to the shear direction and a cluster of [010] axes aligning subnormal to the shear plane, that is, the A-type fabric (Jung et al., 2006; Jung & Karato, 2001b). In all samples except for the anhydrous Fo_{50} sample (PT248), a very weak cluster of [001] axes occurs, aligned 30°–60° from shear plane antithetic to shear direction. This cluster becomes weaker with increasing radius.

Converting radius to shear strain and averaging the shape factor, *K*, for the same strain, plots of fabric shape versus local shear strain, as illustrated in Figure 9, provide a more quantitative measurement of the evolution of fabric shape. The distributions of [100] axes form clusters at very small strains and become more

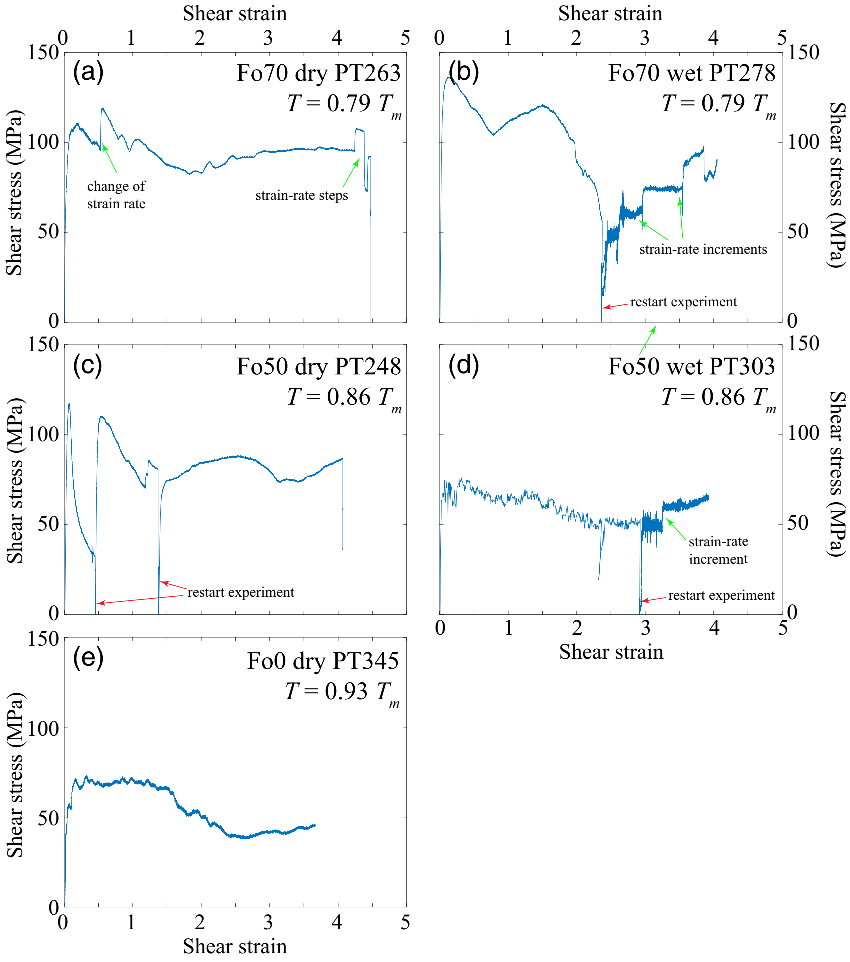

Figure 3. Stress-strain curves for all experimental runs. (a) PT263. (b) PT278. (c) PT248. (d) PT303. (e) PT345.

clustered as strain increases. The distributions of [010] axes form girdles at small strains, become more girdled as strain increases to ∼1, and then become less girdled as strain increases further. The distributions of [001] axes evolve differently in different samples. In the anhydrous Fo_{70} sample, the value of K starts above 1, decreases with increasing strain for $\gamma < 2.5$, and increases slightly with increasing strain for $\gamma > 2.5$, but remains below 1. In the hydrous Fo_{70} sample, the value of K starts above 1 and decreases with increasing strain. In Fo_{50} samples, the value of K starts below 1 and slightly increases with increasing strain. In the Fo_0 sample, the value of K varies between 0.9 and 3.

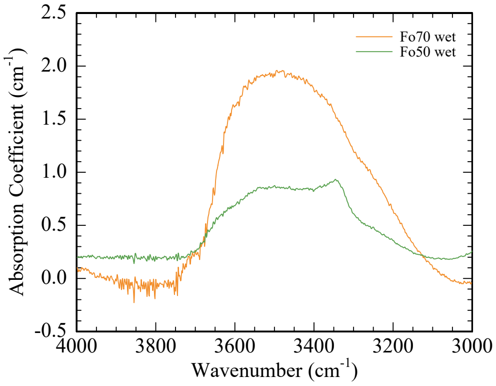

Figure 4. Absorption coefficient versus wavenumber from FTIR analyses of two hydrous samples. Orange is Fo_{70} (PT278). Green is Fo_{50} (PT303).

3.3.2. Iron-Content Series

In samples deformed under anhydrous conditions, at a given strain, the fabric in the Fo_{70} sample is the weakest and the fabrics in the Fo_{50} and Fo_0 samples have similar strengths. In samples deformed under hydrous conditions, at similar strains, the fabric in the Fo_{70} sample is weaker than the fabric in the Fo_{50} sample. At similar strains, the [010]-axis distribution is more clustered in samples with higher iron content, as illustrated in Figure 9b. Note that samples with a higher iron content are also deformed at a higher homologous temperature.

To compare fabrics amongst samples, consider the fourth group of pole figures ($\gamma = 2.9 - 3.5$) for each anhydrous sample. For the Fo_{70} sample

(PT263, Figure 5a), [010] axes form a girdle subnormal to the shear direction. For the Fo_{50} sample (PT248, Figure 6a), [010] axes form a diffuse cluster elongated subnormal to the shear direction. For the Fo_0 sample (PT345, Figure 7), [010] axes form a strong, round cluster normal to the shear plane, with a weak concentration of [010] axes lying in the shear plane subnormal to the shear direction. However, this correlation between the distribution of [010] axes and iron content is not observed in the distributions of [100] and [001] axes. At similar strains, the distribution of [100] axes in Fo_{50} samples is the most clustered, and that in Fo_0 sample is least clustered (Figure 9a). At similar strains, the distribution of [001] axes in Fo_0 sample is the least girdled (Figure 9c). For $\gamma < 2.5$, the distribution of [001] axes in Fo_{50} samples is the most girdled; while for $\gamma > 2.5$, those in Fo_{50} and Fo_{70} samples are similar in shape.

3.3.3. Water-Content Series

The two samples deformed under hydrous conditions exhibit the same CPO pattern as the samples deformed under anhydrous conditions. At the same strain, fabric strengths are similar in anhydrous and hydrous samples (Figure 8a). At the same strain, fabric shapes for all axes are also similar in anhydrous and hydrous samples (Figure 9).

3.4. Seismic Anisotropy

The evolution of radial seismic anisotropy with shear strain is presented in Figure 8b. In all samples, the value of radial anisotropy increases from ~1 to ~1.15 with increasing strain. In each case, the slope of the curve decreases with increasing strain with the curve becoming roughly flat as strain approaches its maximum value. For the same strain in the range of $0.5 < \gamma < 3$, the value of radial anisotropy in the Fo_0 sample is the largest, and values of radial anisotropy in Fo_{70} samples are smallest. For the same iron content, the radial anisotropy of anhydrous and hydrous samples exhibits similar values and trends.

3.5. Recrystallized Grain Sizes

Orientation maps and dynamically recrystallized grain-size distributions for representative areas near the axial center and close to the outer edge are presented in Figure 10, and grain sizes of dynamically recrystallized grains at different radii are presented in Figures 11a and 11b. In all samples, grain sizes are larger near the axial center than close to the outer edge, that is, grain size decreases with increasing radius. At the same radius, the grain size in samples with higher iron content is larger than that in samples with lower iron content, and the grain size in hydrous samples is larger than that in anhydrous samples with the same iron content. Subgrain boundaries and intragranular distortions are observed across the whole radius. In all selected regions, the distributions of grain size are skewed, with a peak at finer grain sizes and a tail extending to coarser grain sizes. The grain-size distributions at regions close to the outer edge are approximately log-normal, as demonstrated by the fitted curves in Figure 10. Comparatively, the grain-size distributions near the axial center are not as well fit by log-normal distributions (see supporting information Figure S2 for grain-size distributions on a logarithmic scale). The geometric mean is always smaller than the arithmetic mean and is closer to the peak of the grain-size distribution. The difference between the arithmetic mean and the geometric mean is smaller when the distribution of grain sizes is tighter (smaller standard deviation). To make a statistically reliable analysis, a minimum number of 433 grains should be measured (Lopez-Sanchez & Llana-Fúnez, 2015). Thus, regions with fewer than 433 grains, for example, Figures 10c and 10e, were not used for further analyses in the Discussion section.

4. Discussion

4.1. Slip Systems

For all samples, CPOs are characterized by a cluster of [100] axes parallel to the shear direction and girdles of [010] and [001] axes subnormal to the shear direction, that is, D-type fabrics, at lower strains, and a cluster of [100] axes parallel to the shear direction and a cluster of [010] axes subnormal to the shear plane, that is, A-type fabrics, at higher strains. Moreover, during our experiments, stresses were always between 50 and 100 MPa, well below the 350–400 MPa reported for the stress transition between the A- and D-type fabrics

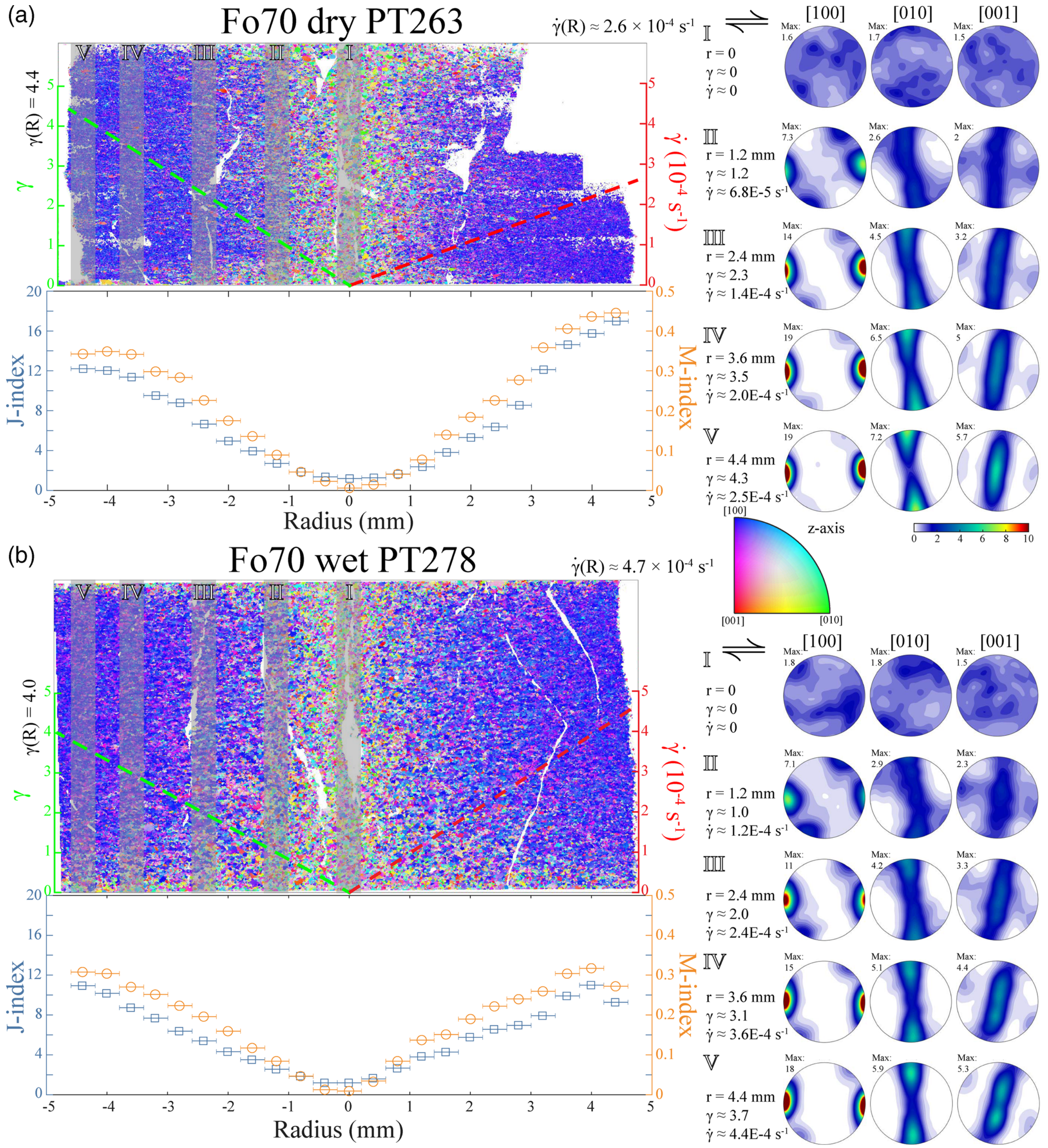

Figure 5. CPOs of Fo_{70} samples deformed under (a) anhydrous (PT263) and (b) hydrous (PT278) conditions. In each panel, an orientation map for the radial section of the sample is presented in the top left, a plot of CPO strength versus radius is presented in the bottom left, and distributions of orientations at different radii are presented in the right. Each orientation map is colored by the crystallographic orientation normal to the radial section, that is, parallel to the shear direction, according to the color map. Shear strain and shear strain rate across the radius are plotted on the map using green and red dashed lines, respectively. Below the map, CPO strength characterized by J- (blue squares) and M-indexes (orange circles) is plotted with radius, with horizontal error bars illustrating the range of radius represented by each data point. Radius $r = 0$ corresponds to the location of the torsional axis, which is the center of the map. The x-axis of the plot shares the same scale as the map. For each selected radius, a pole figure representing distributions of orientations of [100], [010], and [001] axes is contoured based on all orientation data in a 0.4-mm wide area around this radius, as illustrated by the shaded stripe on the map. Pole figures are lower-hemisphere projections. The orientation data for the pole figures are rotated 90°, so that the sense of shear for the pole figures is top to the right. The contours on each stereonet are universally colored by their multiples of uniform distribution (MUD), which is illustrated in the color bar. The maximum values of MUD are listed for each stereonet. CPO, crystallographic preferred orientation.

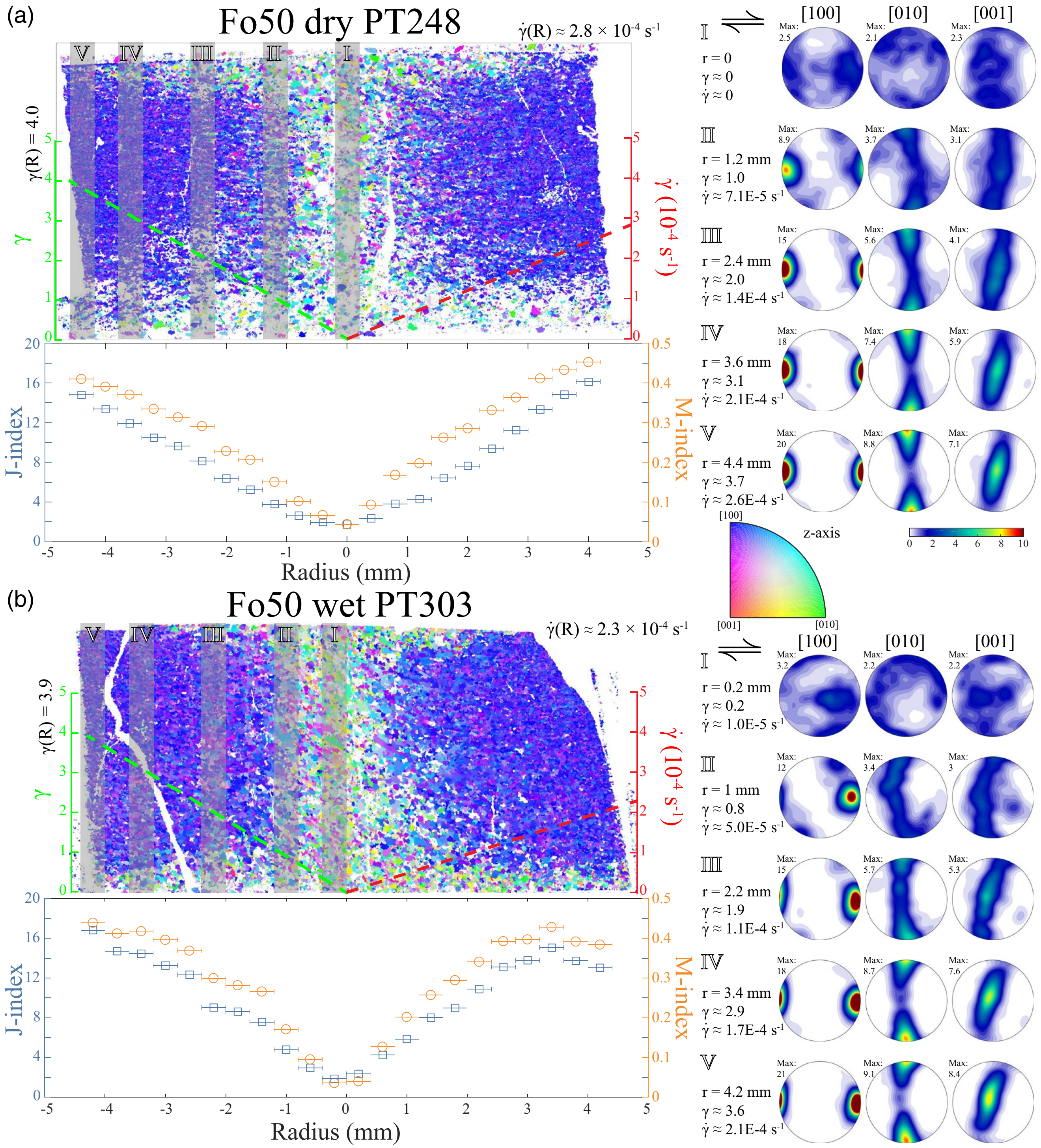

Figure 6. CPOs of Fo_{50} samples deformed under (a) anhydrous (PT248) and (b) hydrous (PT303) conditions. The organization of this figure is the same as Figure 5. Each orientation map is colored by the crystallographic orientation normal to the radial section, that is, parallel to the shear direction, according to the color map. Shear strain and shear strain rate across the radius are plotted on the map using green and red dashed lines, respectively. Below the map, CPO strength characterized by J- (blue squares) and M-indexes (orange circles) is plotted with radius, with horizontal error bars illustrating the range of radius represented by each data point. Radius $r = 0$ corresponds to the location of the torsional axis, which is the center of the map. The x-axis of the plot shares the same scale as the map. For each selected radius, a pole figure representing distributions of orientations of [100], [010], and [001] axes is contoured based on all orientation data in a 0.4-mm wide area around this radius, as illustrated by the shaded stripe on the map. Pole figures are lower-hemisphere projections. The orientation data for the pole figures are rotated 90°, so that the sense of shear for the pole figures is top to the right. The contours on each stereonet are universally colored by their MUD, which is illustrated in the color bar. The maximum values of MUD are listed for each stereonet. CPO, crystallographic preferred orientation.

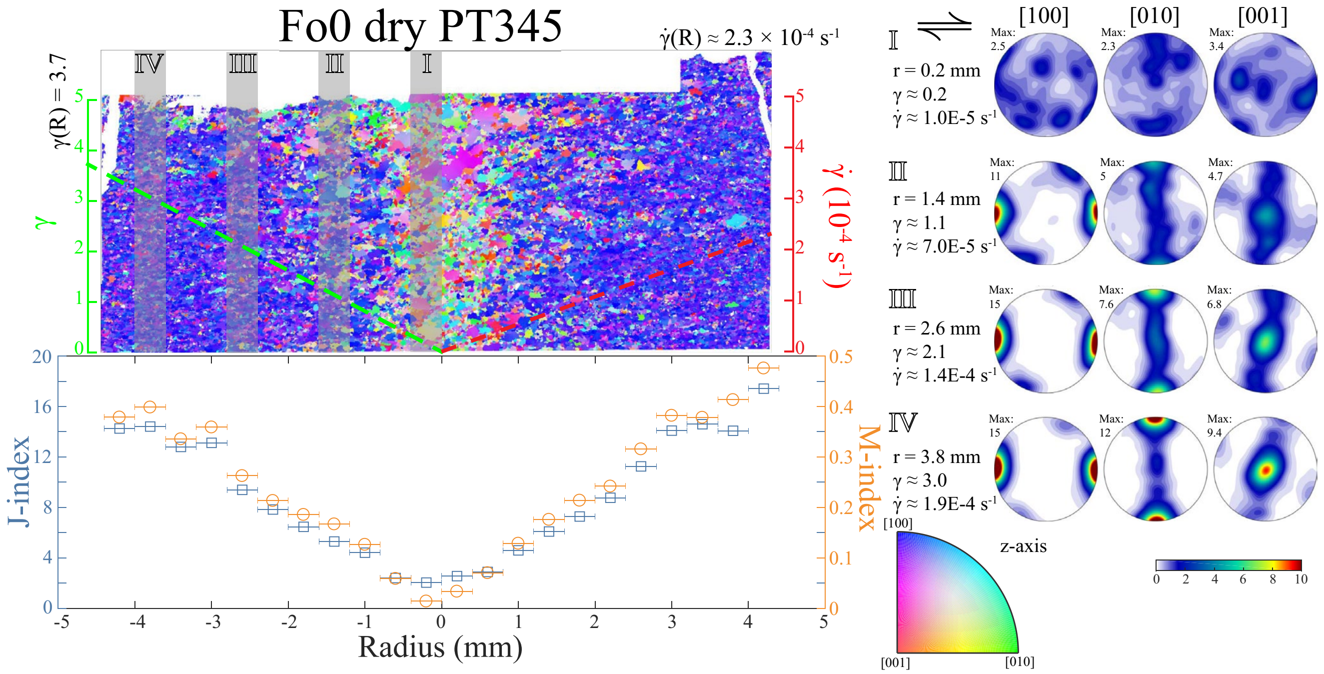

Figure 7. CPOs of the Fo_0 sample (PT345) deformed under anhydrous condition. In the top left, an orientation map is colored by the crystallographic orientation normal to the radial section, that is, parallel to the shear direction, according to the color map. Shear strain and shear strain rate across the radius are plotted on the map using green and red dashed lines, respectively. Below the map, CPO strength characterized by J- (blue squares) and M-indexes (orange circles) is plotted with radius, with horizontal error bars illustrating the range of radius represented by each data point. Radius $r = 0$ corresponds to the location of the torsional axis, which is the center of the map. The x-axis of the plot shares the same scale as the map. In the right, for each selected radius, a pole figure representing distributions of orientations of [100], [010] and [001] axes is contoured based on all orientation data in a 0.4-mm wide area around this radius, as illustrated by the shaded stripe on the map. Pole figures are lower-hemisphere projections. The orientation data for the pole figures are rotated 90°, so that the sense of shear for the pole figures is top to the right. The contours on each stereonet are universally colored by their MUD, which is illustrated in the color bar. The maximum values of MUD are listed for each stereonet. CPO, crystallographic preferred orientation.

at our experimental temperature and pressure (Karato et al., 2008); thus, the change from D-type to A-type fabric is associated with increasing strain. These observations are consistent with those previously reported for anhydrous Fo_{90} and Fo_{50} samples (Hansen et al., 2014). The D-type fabric at low strains is caused by dislocation glide on the {0kl}[100] slip systems (Carter & Ave'Lallemant, 1970), but more specifically, on the (010)[100] and the (001)[100] slip systems (Hansen et al., 2014), as the two slip systems are similar in strength (Bai et al., 1991; Durham et al., 1977; Tielke et al., 2016) and the major dislocations in the {0kl}

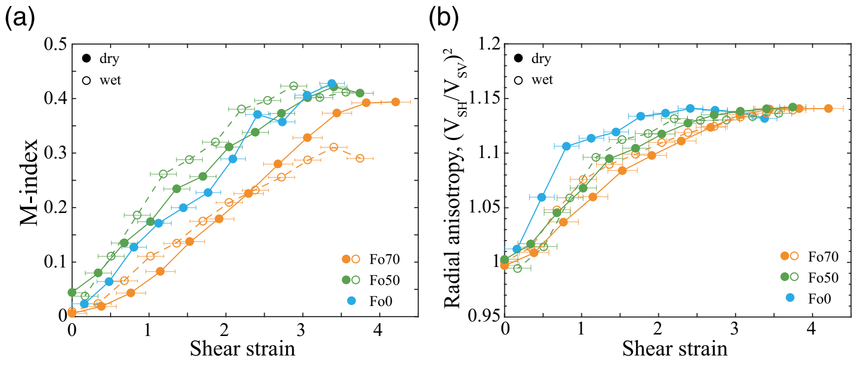

Figure 8. Evolution of fabric strength and radial anisotropy with local shear strain. Orange is Fo_{70}. Green is Fo_{50}. Blue is Fo_0. Solid circles and lines are results for anhydrous samples. Open circles and dashed lines are results for hydrous samples. Horizontal error bars are the range of strain represented by each data point. (a) Plot of M-index versus shear strain. (b) Plot of magnitude of radial anisotropy versus shear strain. Radial anisotropy is calculated assuming the shear plane is horizontal.

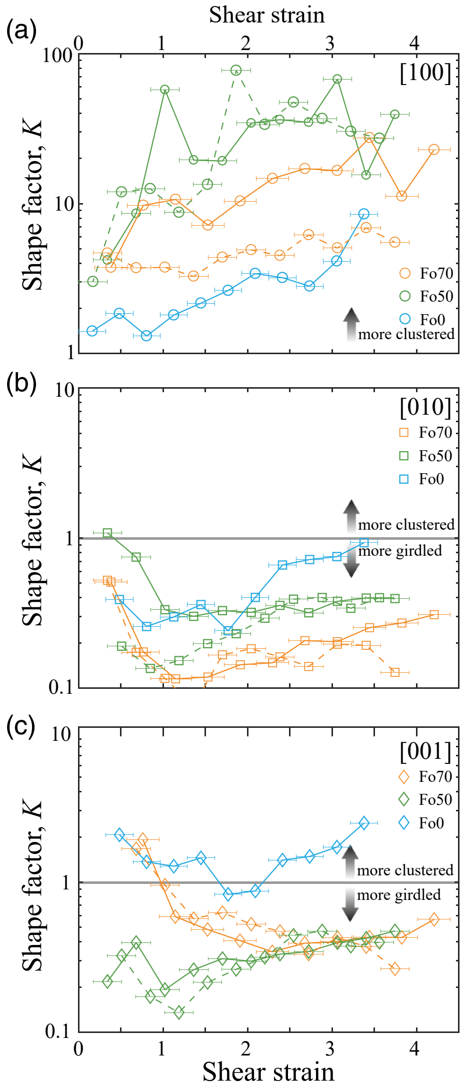

Figure 9. Evolution of fabric shape with local shear strain. Orange is Fo_{70}. Green is Fo_{50}. Blue is Fo_0. Solid lines are results for anhydrous samples. Dashed line are results for hydrous samples. Horizontal error bars indicate the range of strain represented by each data point. (a) Plot of shape factor for the distribution of [100] axes versus strain. (b) Plot of shape factor for the distribution of [010] axes versus strain. The gray horizontal line marks $K = 1$. (c) Plot of shape factor for the distribution of [001] axes versus strain. In panels (b) and (c), the data point at very small strains was removed, as the distributions of axes are quite random such that values of K are also random.

[100] family (Hansen et al., 2014; Wallis et al., 2019). As strain increases, the A-type fabric dominates, indicating that (010)[100] is the weakest slip system. The observed fabric evolution with increasing strain, therefore, is primarily caused by the transition from a combination of the (010)[100] and (001)[100] slip systems to dominantly the (010)[100] slip system.

In addition to the primary cluster of [100] axes aligning parallel to the shear direction, a weak secondary cluster of [100] axes occurs at small radii/low strains. The occurrence of this secondary [100]-axis cluster has been reported for Fo_{90} samples deformed under anhydrous conditions that were characterized by an A-type fabric (Zhang et al., 2000) and accepted as a minor feature of the A-type fabric (Karato et al., 2008). This secondary [100]-axis cluster is sub-perpendicular to the maximum principal compressive stress. Zhang et al. (2000) argued that this secondary cluster is stress controlled. New grains in low-Schmid-factor orientations will have the lowest dislocation densities (Karato, 1987). Because the active systems are mainly (010)[100] and (001)[100], grains with [100] orienting at 90° to the maximum principal stress represent the lowest-Schmid-factor orientations. Thus, grains with this crystallographic orientation grow and consumes other grains via grain boundary migration (Zhang et al., 2000). Because grain boundary migration does not contribute to strain, as strain increases, grain boundary migration contributes less to CPO formation, subgrain rotation contributes more, and the secondary [100]-axis cluster disappears.

In the review of the CPOs of olivine samples naturally and experimentally deformed under anhydrous conditions, Skemer and Hansen (2016) reported that the secondary cluster of [100] axes moves toward the primary cluster of [100] axes with increasing strain. For example, in samples experimentally deformed in direct shear, the angle between secondary and primary clusters of [100] axes decreases from ~45° at $\gamma < 0.2$ to 0° at $\gamma > 1.5$ (Zhang & Karato, 1995). However, such a decrease was not observed in our samples. Rather, in our samples, with increasing strain, the weak secondary cluster of [100] axes roughly remains at 60–70° to the primary cluster of [100] axes through $\gamma = 1$–4. Similarly, in samples experimentally deformed in torsion by Skemer et al. (2011), the angle between the two clusters of [100] axes only decreases slightly from mid-50° to mid-40° with strain increasing from $\gamma \approx 1.2$ to 3.5. The difference in the deformation kinematics, direct shear versus torsion, is likely the cause for the difference in the change in orientation of the secondary cluster, as direct shear is a combination of compression and simple shear.

The observation that the A-type fabric dominates at high strains in all samples suggests that (010)[100] is the weakest slip system over a wide range of iron content at our experimental conditions, from San Carlos olivine, Fo_{90}, to fayalite, Fo_0. No correlation was found between the evolution of fabric shape (Figure 9) and iron content, suggesting that variations in iron content do not change the relative strengths of primary slip systems in olivine, consistent with results from deformation experiments on single crystals as reported by Kohlstedt and Ricoult (1984).

Before looking into the CPOs of samples deformed under hydrous conditions, we estimate the OH concentration in these samples. Under water-saturated conditions, as in our experiments, at 300 MPa and 1200°C the OH concentration in single crystals of San Carlos olivine (ca. Fo_{90}) is ~300 ppm H/Si (Bai & Kohlstedt, 1992; Tasaka et al., 2016; Zhao et al., 2004) using the Paterson (1982) OH-infrared calibration. Based on the results of a study by Withers et al. (2011), water solubility in Fo_{70} and Fo_{50} is ~1.6 times and ~2.2 times that in Fo_{90}, respectively. That is, under water-saturated conditions, the OH concentration in our samples

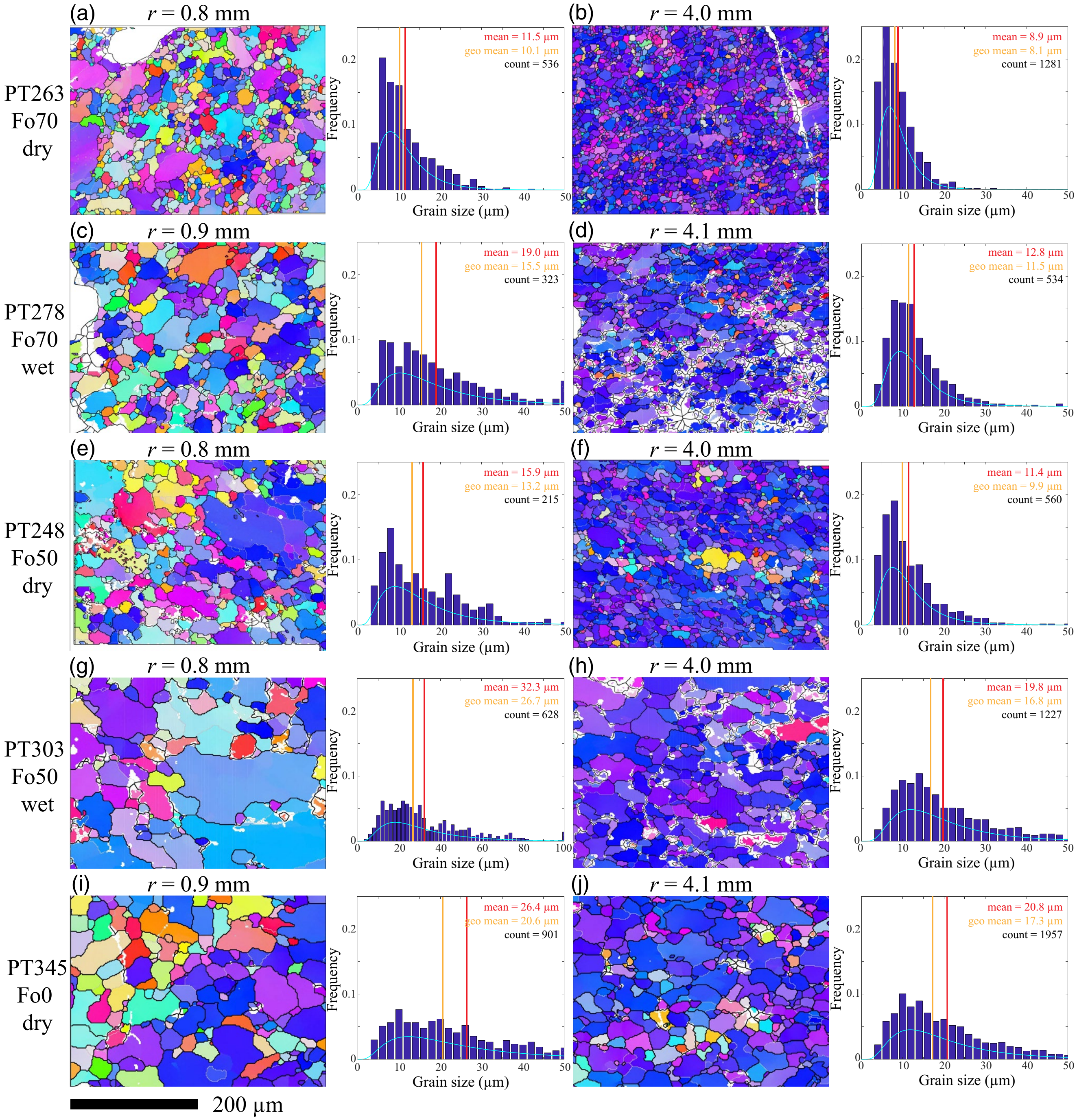

Figure 10. Orientation maps and grain-size distribution histograms for selected regions in all samples. Regions near the axial center are in the left column, and regions close to the outer edge are in the right column. In each panel, an orientation map colored by the crystallographic orientation parallel to the shear direction is on the left, and a histogram of the distribution of grain size is on the right. In the map, grain boundaries, characterized by a misorientation of ≥10°, are black, and subgrain boundaries, characterized by a misorientation of <10° and ≥2°, are gray. Unindexed spots are white. Color maps are the same as in Figures 5–7. Maps are subareas of the whole mapped area (except for PT263). The whole mapped area was used to calculate grain size. In the histogram, the red line marks the arithmetic mean and the orange line marks the geometric mean. The blue curve is a log-normal fit of the grain-size distribution. The number of grains used to calculate the means is also provided in each histogram. Grain size distributions are plotted in logarithm scale in Figure S2.

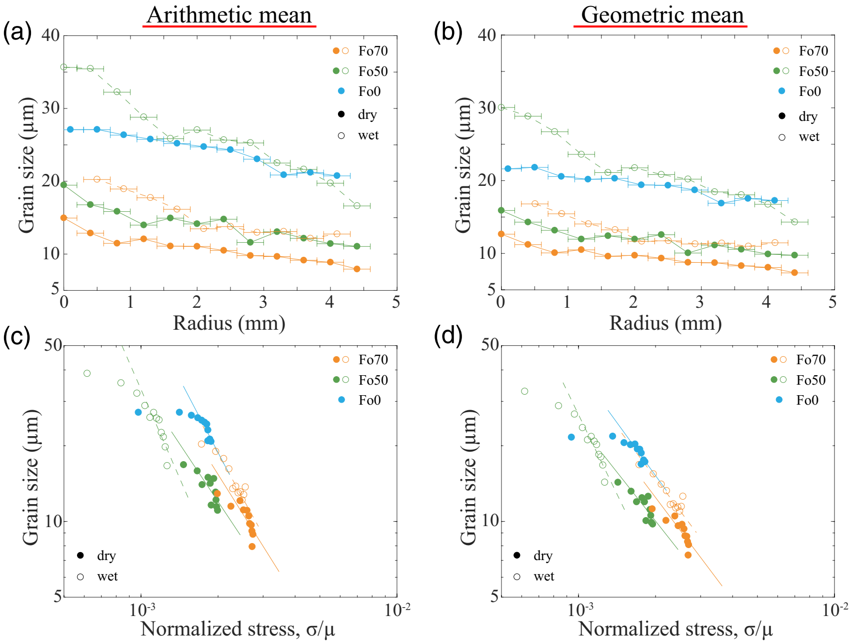

Figure 11. Evolution of grain size with (a) and (b) radius and (c) and (d) normalized stress. In the left column, average grain sizes are calculated as arithmetic means; in the right column, average grain sizes are calculated as geometric means. Orange is Fo_{70}. Green is Fo_{50}. Blue is Fo_0. Solid circles and lines are results for anhydrous samples. Open circles and dashed lines are results for hydrous samples. In (c) and (d), normalized equivalent stresses are calculated using the flow laws in Equations 5 and 6. $p_{O_2} = 10^{-3}$ Pa is used in Equation 5. $f_{H_2O} = 300$ MPa is used in Equation 6. Solid and dashed lines are the linear fits for data points that are (1) taken at $r > 1$ mm, and (2) averaged based on more than 400 grains. Slopes are presented in Table 3.

are ~500 ppm H/Si for Fo_{70} and ~700 ppm H/Si for Fo_{50}. We note that OH solubilities cannot be calculated from our FTIR spectra, because the broad band associated with molecular water swamps the signal from OH groups.

The CPOs of our samples deformed under hydrous conditions exhibit both similarities to and differences from the CPOs of hydrous Fo_{50} samples reported by Tasaka et al. (2016). CPOs at $\gamma \leq 2$ in our hydrous Fo_{70} (PT278) and Fo_{50} (PT303) samples are very similar to the CPOs in samples deformed to $\gamma = 2.4$ (PT954) and $\gamma = 3.0$ (PT939) in Tasaka et al. (2016). Note that the difference in the orientations of the [001]-axis girdles between this study and Tasaka et al. (2016) is due to different projections of crystallographic orientations (see Wallis et al., 2019, for correction of the projection). All of our pole figures are plotted using lower-hemisphere projection, as was done as in many previous studies (e.g., Hansen et al., 2014). Because the two slip systems (001)[100] and (100)[001] are similar in strength at $T = 1423–1473$ K for Fo_{90} deformed under anhydrous (Durham & Goetze, 1977; Tielke et al., 2016) and hydrous conditions (Wallis et al., 2019) and because iron content does not affect the relative strengths of the primary slip systems (an assumption in Tasaka et al. (2016), but an interpretation in this study), Tasaka et al. (2016) concluded that these CPOs resulted from slip on a combination of the (010)[100], (001)[100], and (100)[001] slip systems, in which the operation of the (010)[100] and (001)[100] slip systems leads to the D-type fabric and operation of the (100)[001] slip system leads to the weak [001]-axes cluster sub-parallel to shear direction. This explanation applies to our hydrous samples at lower strains ($\gamma \lesssim 2$). With increasing strain, in our samples, the (010)[100] slip system contributed more than the (001)[100] slip system to the CPO, leading to an A-type fabric at higher strains ($\gamma \gtrsim 3$); however, in samples of Tasaka et al. (2016), the (001)[100] and (100)[001] slip systems dominated, leading to bimodal distributions of [100] and [001] axes. In our samples, although the (010)[100], (001)[100], and (100)[001] slip systems were activated, the (010)[100] slip system remained the weakest, thus dominating CPO development at high strains. Considering the estimated water contents in our samples, these results suggest the A-type fabric dominates over a broader range of water content in iron-rich olivines than in Fo_{90} (Jung et al., 2006).

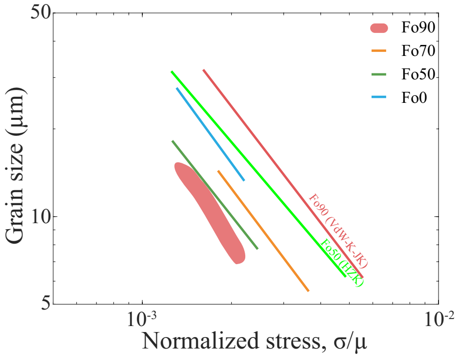

Figure 12. Comparison with previously reported piezometric relationships for anhydrous olivines. The red shaded region represents the data for anhydrous Fo_{90} deformed in torsion at 1523 K (Meyers, 2020). The light green line marks the piezometer for anhydrous Fo_{50} reported by Hansen et al. (2012a) with a slope of −1.2. The solid red line marks the piezometer for anhydrous Fo_{90} ($\mu = 63.5$ GPa) reported by Van der Wal et al. (1993) and Jung and Karato (2001a) with a slope of −1.33 (data of Karato et al. (1980) are included in Van der Wal et al. (1993)).

The CPOs of our samples deformed under hydrous conditions differ from the CPOs of Fo_{90} samples deformed under hydrous condition in previous studies that were carried out at higher confining pressures, $P \geq 500$ MPa, and thus at higher water fugacity, $f_{H_2O} > 600$ MPa, and higher OH concentrations, $C_{OH} > 1000$ ppm H/Si (Jung et al., 2006; Jung & Karato, 2001b; Katayama et al., 2004). Jung et al. (2006) reported that, at low differential stresses (similar to those used in our study), the easiest slip system changes from (010)[100] at low OH content, to (001)[100] at moderate OH content, and then to (100)[001] at high OH content. The water content in our samples, independent of iron content, must lie below that required to cause a change in the dominant slip system from (010)[100] to (001)[100].

4.2. Seismic Anisotropy

The value of radial anisotropy increases from ∼1 at $\gamma = 0$ to ∼1.15 at higher strains in all samples. Although the values of radial anisotropy in samples with different iron contents increase at different rates with increasing strain, all of the values converge to the same maximum at $\gamma > 3.5$. Similarly, previous data for radial anisotropy of Fo_{90} and Fo_{50} also reached a maximum of ∼1.15 at large strains, $\gamma \approx 5$ (Hansen et al., 2014). Therefore, olivines with different iron contents exhibit the same radial anisotropy at a shear strain as low as 3.5, demonstrating that seismic anisotropy in natural olivine aggregates can be well-modeled using CPO data obtained from laboratory experiments on iron-rich olivine.

4.3. Recrystallized Grain Size and Stress

The relationship between dynamically recrystallized grain size, d_{rex}, and stress provides an important tool for estimating the stress experienced by a naturally deformed rock. This relationship can be analyzed in terms of either the piezometer (Twiss, 1977) or the wattmeter (Austin & Evans, 2007) formalism. Here, because of the lack of information on grain growth kinetics as a function of iron content in olivine, information that is critical for the wattmeter, we focus on the piezometer in the form (Hirth & Kohlstedt, 2015)

$$d_{\mathrm{rex}} = \frac{2\gamma_{\mathrm{gb}}}{\alpha\mu A}\left(\frac{\sigma}{\mu}\right)^{-q}, \tag{13}$$

where γ_{gb} is the average grain boundary energy and α is a geometrical constant associated with the interactions between dislocations. The material-dependent parameters A and q enter through the empirical relationship between dislocation density, ρ, and stress (Twiss, 1977)

$$\rho b^2 = A\left(\frac{\sigma}{\mu}\right)^q. \tag{14}$$

For our samples, recrystallized grain sizes at different radii were measured from the orientation maps in Figures 5–7. Stresses at different radii were calculated using Equations 5–8. Based on Figure 8, M-index, an indicator for CPO development, increases faster with increasing strain in Fo_{50} than in Fo_{70} and Fo_0, such that, the critical strain for CPO development, estimated to be 1 for Fo_{50} (Hansen et al., 2012a), should be larger for Fo_{70} and Fo_0. Consider the M-index at $\varepsilon_c = 1$ for Fo_{50}, and to achieve a similar M-index, ε_c is estimated to be 1.5 for Fo_{70} and 1.1 for Fo_0. Therefore, a piezometric relationship can be determined for each sample.

It is worth noting that this analysis is based on two assumptions. First, for each sample, the radial stress distribution calculated from the published flow law determined for that sample (Zhao et al., 2009, 2018) is accurate. Based on microstructural observations, dynamic recrystallization by subgrain rotation widely occurred, demonstrating that dislocations played a major role in deformation of our samples. This observation is in good agreement with our interpretation based on the mechanical data that samples were deformed in disGBS for anhydrous samples and dislocation creep for hydrous samples. Moreover, since the samples used to determine the flow laws were the same as those deformed in our torsion experiments, the flow laws should provide a good description of the rheological properties of our samples. Second, the measured grain size represents the recrystallized grain size. As described in the Methods section, recrystallized grains were distinguished using the GOS-thresholding method developed for quartz by Cross et al. (2017). However, if grains in certain orientations have lower GOS values than those in other orientations, and thus, are preferentially picked as "recrystallized," this GOS-thresholding method cannot stand. In the application of this method, it is important to ensure that grain orientation does not influence the GOS. A plot of GOS versus Schmid factor of the (010)[100] slip system reveals that the value of GOS slightly increases by 0.4° as the Schmid factor increases from 0 to 0.5 (see Figure S3). This observation suggests that there is at most a weak effect of grain orientation on the residue intragranular misorientations. Therefore, the GOS-thresholding method could be used without causing significant bias. Another concern is whether the grain size observed in a radial section is the same as that observed in the corresponding tangential section of a torsion sample. A comparison between the microstructure from a radial section and a tangential section from similar radii reveals very similar average grain sizes (see Figure S4). Thus, we conclude that the grain sizes observed on radial sections are representative.

Plots of dynamically recrystallized grain size versus normalized stress for all of our samples are presented in Figures 11c and 11d using the arithmetic and geometric mean values of grain size, respectively. Three general observation warrant comment.

First, except for hydrous Fo_{50}, values of q determined from fits of the results using the arithmetic mean for each sample in Figures 11c to Equation 13 lie in the range $1.5 \leq q \leq 1.9$, as reported in Table 3. This result is slightly higher than the values for q previously reported for Fo_{90} and Fo_{50} (e.g., Karato et al., 1980; Hansen et al., 2012a; Hirth & Kohlstedt, 2015). Except for hydrous Fo_{50}, values of q determined from fits of the results using the geometric mean for each sample in Figures 11d to Equation 13 lie in the range $1.3 \leq q \leq 1.4$. This result is in good agreement with values for q obtained under hydrous and anhydrous conditions for samples of Fo_{90} (Hirth & Kohlstedt, 2015; Jung & Karato, 2001a; Karato et al., 1980; Van der Wal et al., 1993) and under anhydrous conditions for samples of Fo_{50} (Hansen et al., 2012a).

Second, at a given stress, the grain size of a sample deformed under anhydrous conditions is approximately equal to that of a sample of the same composition deformed under hydrous conditions (Figures 11c and 11d). A similar result was reported for samples of Fo_{90} deformed at $f_{H_2O} \lesssim 300$ MPa (Jung & Karato, 2001a; Van der Wal et al., 1993). At $f_{H_2O} \gtrsim 500$ MPa, the dynamically recrystallized grain size exceeds that for samples deformed under anhydrous conditions with grain size increasing with increasing water content (Jung & Karato, 2001a).

Third, at a given stress under anhydrous conditions, the grain size is larger for the sample of Fo_0 than for samples of Fo_{70} and Fo_{50} (Figures 11c and 11d). To extend this comparison over a wider range of iron content, the piezometer determined from radial sections of Fo_{90} samples deformed in torsion in our lab under anhydrous conditions (Meyers, 2020) is plotted with our results in Figure 12. Inclusion of the piezometer for Fo_{90} reveals a clear trend of increasing recrystallized grain size with increasing iron content. The fact that olivine samples with higher iron contents are deformed at higher homologous temperatures is unlikely the cause for this trend. Previous studies demonstrate for Fo_{90} olivine that the material parameters in Equation 13 do not vary significantly over a wide range of temperature (Karato et al., 1980; Van der Wal et al., 1993). Thus, we attribute this trend to the effect of iron.

Some insight into the reason that iron influences the relationship between dynamically recrystallized grain size and normalized stress comes from considering the terms that make up Equation 13. In this piezometric relation, iron potentially affects γ_{gb}, μ, A, and/or q. Grain boundary energy for olivine is largely insensitive to iron content (Hiraga et al., 2010). In contrast, the shear modulus decreases with increasing iron content (Bass, 1995, Table 7), such that grain size would increase with increasing content. The modulus for Fo_{90} is a factor of ~1.7 larger than the modulus of Fo_0 at our experimental temperatures (1200°C and 1100°C, respectively). However, at a given stress, the grain size of the Fo_0 sample is ~2.5 times larger than the grain size of Fo_{90} samples, suggesting that the dislocation density—stress relationship in Equation 14, which is used in deriving Equation 13, accounts for at least part of the dependence of grain size on iron content.

A comparison of our results obtained on samples of Fo_{50} and Fo_{90} deformed under anhydrous conditions with published piezometers is also presented in Figure 12. For Fo_{50}, the piezometer determined in this study is in very good agreement with that obtained by Hansen et al. (2012a), which was based on analyses of tangential sections of a series of samples deformed to high strain in torsion. In contrast, at a given normalized stress, recrystallized grain sizes for anhydrous Fo_{90} calculated from the piezometers determined by Van der Wal et al. (1993) and Jung and Karato (2001a) are significantly larger than those calculated using the piezometer of Meyers (2020). This discrepancy is likely due to differences in the methods used for measuring grain size. Piezometers reported for Fo_{90} prior to our study used grain sizes measured by optical microscopy. In the present paper, grain size was determined by EBSD analyses. As demonstrated by Hansen et al. (2011), average grain sizes determined optically are often significantly larger than those determined by EBSD, likely accounting for the offset between the two piezometers for Fo_{90} olivine.

In addition, the value of q for hydrous Fo_{50} sample is larger than the values for the other samples. Additional experimental work is needed to determine if this observation is robust or if it simple reflects sample-to-sample variations.

4.4. Arithmetic Mean and Geometric Mean

Values of grain size calculated from the arithmetic mean and the geometric mean were compared in several regions of each sample as illustrated in Figure 10. The geometric mean is always closer to the frequency peak of the grain-size distribution than the arithmetic mean, and the difference between the two means varies with the grain-size distribution. Several previous studies have proposed that the geometric mean provides a more representative estimate of the average grain size (Lopez-Sanchez, 2020; Lopez-Sanchez & Llana-Fúnez, 2015; Ranalli, 1984; Warren et al., 2008). However, the geometric mean is seldom used in the literature, because one key in processing a paleopiezometer is the reproducibility across studies (e.g., Stipp et al., 2010), and many studies prior to 2000 used the arithmetic mean.

Here we compare the grain size-stress relationships derived using both methods in Figures 11c and 11d. For the same sample, the magnitude of the exponent q in Equation 13 is smaller using the geometric mean than using the arithmetic mean. It seems that the deviation between the arithmetic mean and the geometric mean is larger if the grain-size distribution does not fit well to a log-normal distribution. However, the values of q obtained using the geometric means have a smaller deviation than those obtained using the arithmetic means. This result suggests that geometric mean may provide more consistency in the grain size analyses.

Table 3
Parameters in the Piezometric Relationship for Each Sample

Composition	Hydrous/anhydrous	μ (GPa)	Arithmetic mean q	Geometric mean q
Fo_{70}/Fa_{30}	Anhydrous	56.7	1.6 ± 0.5	1.4 ± 0.4
	Hydrous		1.8 ± 0.2	1.4 ± 0.2
Fo_{50}/Fa_{50}	Anhydrous	51.4	1.5 ± 0.5	1.3 ± 0.4
	Hydrous		2.3 ± 0.5	2.1 ± 0.4
Fo_{0}/Fa_{100}	Anhydrous	37.3	1.9 ± 0.5	1.4 ± 0.4

4.5. Geological Applications

Although CPOs and the associated seismic anisotropy of sheared iron-rich olivine, typically Fo_{50}, have been used to simulate those in natural olivine, Fo_{90} (Hansen et al., 2012a, 2016, 2014; Tasaka et al., 2016; Wallis et al., 2019), whether or not the seismic anisotropy is the same in deformed Fo_{50} as in deformed Fo_{90} has not been tested. Our experiments reveal that, in olivines with different iron contents, deformation-induced CPOs are the same and the strength of seismic anisotropy reaches the same maximum after a shear strain of ~3.5. In addition, the evolution of radial seismic anisotropy for deformed olivine is not highly sensitive to iron content such that the experimental results in Figure 8b should provide a good approximation for naturally deformed, olivine-rich rocks as proposed by Hansen et al. (2014). Moreover, our results also suggest that seismic anisotropy in the mantle of Mars, if caused by the CPO of olivine, can be interpreted based on our understanding of the mantle of Earth, even though the iron content in olivine is different on Mars than on Earth.

5. Conclusions

- In olivines with different iron contents deformed at a confining pressure of 300 MPa, CPOs transition from D-type fabrics, induced by dislocation glide on both the (010)[100] and (001)[100] slip systems, at low strains, to A-type fabrics, induced by dislocation glide on the (010)[100] slip system, at high strains.
- Variations in the iron content do not change the relative strengths of the primary slip systems in olivine, which are the (010)[100], (001)[100], and (100)[001]. CPOs in iron-rich olivines can be used to simulate CPOs in natural olivine, Fo_{90}.
- Olivines with different iron contents exhibit the same strength of seismic anisotropy at a shear strain as low as 3.5, demonstrating that seismic anisotropy in natural olivine aggregates can be well-modeled using CPO data obtained from laboratory experiments on iron-rich olivine.
- The value of the stress exponent, q, in the piezometeric relationship lies between 1.3 and 1.4 over the range of iron contents investigated, similar to the previously reported values of 1.2–1.4.

Acknowledgments
The authors thank to Lars Hansen, Zachary Michels, Amanda Dillman, Cameron Meyers and Harison Wiesman for stimulating discussions. The authors are also grateful to Lars Hansen and Zachary Michels for sharing their codes for analyzing orientation data obtained by EBSD. Comments from Andrew Cross, Haemyeong Jung, an associate editor and two anonymous reviewers are appreciated. This research was supported by the Key Research Program of the Institute of Geology and Geophysics, CAS, grant IGGCAS-201905 (to CQ), National Key R&D Program of China grants 2018YFC1504203 and SQ2017YFSF040025 (to YHZ), KOPRI project PE21050 (to DK), and NSF grant EAR-1755805 (to DLK). EBSD analyses were done in the SEM laboratory at Korea Institute for Rare Metals (KIRAM), and in the laboratory at Beijing office of Oxford Instruments company.

Data Availability Statement

Data can be found in this repository: https://doi.org/10.6084/m9.figshare.11838936.v1.

References

Abramson, E. H., Brown, J. M., Slutsky, L. J., & Zaug, J. (1997). The elastic constants of San Carlos olivine to 17 gpa. *Journal of Geophysical Research*, *102*(B6), 12253–12263.

Austin, N. J., & Evans, B. (2007). Paleowattmeters: A scaling relation for dynamically recrystallized grain size. *Geology*, *35*(4), 343–346.

Bachmann, F., Hielscher, R., & Schaeben, H. (2010). Texture analysis with MTEX – Free and open source software toolbox. *Solid State Phenomena*, *160*, 63–68.

Bachmann, F., Hielscher, R., & Schaeben, H. (2011). Grain detection from 2d and 3d EBSD data – Specification of the MTEX algorithm. *Ultramicroscopy*, *111*(12), 1720–1733.

Bai, Q., & Kohlstedt, D. L. (1992). Substantial hydrogen solubility in olivine and implications for water storage in the mantle. *Nature*, *357*(6380), 672–674.

Bai, Q., Mackwell, S. J., & Kohlstedt, D. L. (1991). High-temperature creep of olivine single crystals 1. mechanical results for buffered samples. *Journal of Geophysical Research*, *96*(B2), 2441–2463.

Bass, J. D. (1995). Elasticity of minerals, glasses, and melts. In T. J. Ahrens (Ed.), *Mineral physics and crystallography: A handbook of physical constants* (Vol. *2*, pp. 45–63). American Geophysical Union.

Bertka, C. M., & Fei, Y. (1997). Mineralogy of the martian interior up to core-mantle boundary pressures. *Journal of Geophysical Research*, *102*(B3), 5251–5264.

Borch, R. S., & Green, H. W. (1989). Deformation of peridotite at high pressure in a new molten salt cell: Comparison of traditional and homologous temperature treatments. *Physics of the Earth and Planetary Interiors*, *55*(3–4), 269–276.

Bowen, N. L., & Schairer, J. F. (1935). The system mgo-feo-sio$_2$. *American Journal of Science*, *170*, 151–217.

Bunge, H. J. (1982). *Texture analysis in materials science: Mathematical methods*. Butterworths London.

Carter, N. L., & Ave'Lallemant, H. G. (1970). High temperature flow of dunite and peridotite. *The Geological Society of America Bulletin*, *81*(8), 2181–2202.

Chopra, P. N., & Paterson, M. S. (1981). The experimental deformation of dunite. *Tectonophysics*, *78*(1–4), 453–473.

Cooper, R. F., & Kohlstedt, D. L. (1986). Rheology and structure of olivine-basalt partial melts. *Journal of Geophysical Research: Solid Earth*, *91*(B9), 9315–9323.

Cross, A. J., Prior, D. J., Stipp, M., & Kidder, S. (2017). The recrystallized grain size piezometer for quartz: An EBSD-based calibration. *Geophysical Research Letters*, *44*(13), 6667–6674.

de Bresser, J., Ter Heege, J., & Spiers, C. (2001). Grain size reduction by dynamic recrystallization: Can it result in major rheological weakening?. *International Journal of Earth Sciences*, *90*(1), 28–45.

Deer, W. A., Howie, R. A., & Zussman, J. (1966). *An introduction to the rock forming minerals*. London: Longman.

Durham, W. B., & Goetze, C. (1977). Plastic flow of oriented single crystals of olivine: 1. mechanical data. *Journal of Geophysical Research*, *82*(36), 5737–5753.

Durham, W. B., Goetze, C., & Blake, B. (1977). Plastic flow of oriented single crystals of olivine: 2. Observations and interpretations of the dislocation structures. *Journal of Geophysical Research*, *82*(36), 5755–5770.

Hansen, L. N., Warren, J. M., Zimmerman, M. E., & Kohlstedt, D. L. (2016). Viscous anisotropy of textured olivine aggregates, part 1: Measurement of the magnitude and evolution of anisotropy. *Earth and Planetary Science Letters*, *445*, 92–103.

Hansen, L. N., Zhao, Y.-H., Zimmerman, M. E., & Kohlstedt, D. L. (2014). Protracted fabric evolution in olivine: Implications for the relationship among strain, crystallographic fabric, and seismic anisotropy. *Earth and Planetary Science Letters*, *387*, 157–168.

Hansen, L. N., Zimmerman, M. E., & Kohlstedt, D. L. (2011). Grain boundary sliding in san carlos olivine: Flow law parameters and crystallographic-preferred orientation. *Journal of Geophysical Research: Solid Earth*, *116*(B8), B08201.

Hansen, L. N., Zimmerman, M. E., & Kohlstedt, D. L. (2012a). The influence of microstructure on deformation of olivine in the grain-boundary sliding regime. *Journal of Geophysical Research*, *117*, B09201.

Hansen, L. N., Zimmerman, M. E., & Kohlstedt, D. L. (2012b). Laboratory measurements of the viscous anisotropy of olivine aggregates. *Nature*, *492*(7429), 415.

Hiraga, T., Tachibana, C., Ohashi, N., & Sano, S. (2010). Grain growth systematics for forsterite±enstatite aggregates: Effect of lithology on grain size in the upper mantle. *Earth and Planetary Science Letters*, *291*(1–4), 10–20.

Hirth, G., & Kohlstedt, D. L. (1995a). Experimental constraints on the dynamics of the partially molten upper mantle: 2. deformation in the dislocation creep regime. *Journal of Geophysical Research*, *100*(B8), 15441–15449.

Hirth, G., & Kohlstedt, D. L. (1995b). Experimental constraints on the dynamics of the partially molten upper mantle: Deformation in the diffusion creep regime. *Journal of Geophysical Research*, *100*(B2), 1981–2001.

Hirth, G., & Kohlstedt, D. L. (2015). The stress dependence of olivine creep rate: Implications for extrapolation of lab data and interpretation of recrystallized grain size. *Earth and Planetary Science Letters*, *418*, 20–26.

Jung, H., & Karato, S.-i. (2001a). Effects of water on dynamically recrystallized grain-size of olivine. *Journal of Structural Geology*, *23*(9), 1337–1344.

Jung, H., & Karato, S.-i. (2001b). Water-induced fabric transitions in olivine. *Science*, *293*(5534), 1460–1463.

Jung, H., Katayama, I., Jiang, Z., Hiraga, T., & Karato, S.-i. (2006). Effect of water and stress on the lattice-preferred orientation of olivine. *Tectonophysics*, *421*(1–2), 1–22.

Kang, H., & Jung, H. (2019). Lattice-preferred orientation of amphibole, chlorite, and olivine found in hydrated mantle peridotites from bjørkedalen, southwestern Norway, and implications for seismic anisotropy. *Tectonophysics*, *750*, 137–152.

Karato, S.-i. (1987). Scanning electron microscope observation of dislocations in olivine. *Physics and Chemistry of Minerals*, *14*(3), 245–248.

Karato, S.-i. (2008). *Deformation of earth materials*. Cambridge University Press.

Karato, S.-i., & Jung, H. (2003). Effects of pressure on high-temperature dislocation creep in olivine. *Philosophical Magazine*, *83*(3), 401–414.

Karato, S.-i., Jung, H., Katayama, I., & Skemer, P. (2008). Geodynamic significance of seismic anisotropy of the upper mantle: new insights from laboratory studies. *Annual Review of Earth and Planetary Sciences*, *36*, 59–95.

Karato, S.-i., Paterson, M. S., & FitzGerald, J. D. (1986). Rheology of synthetic olivine aggregates: Influence of grain size and water. *Journal of Geophysical Research*, *91*(B8), 8151–8176.

Karato, S.-i., & Rubie, D. C. (1997). Toward an experimental study of deep mantle rheology: A new multianvil sample assembly for deformation studies under high pressures and temperatures. *Journal of Geophysical Research: Solid Earth*, *102*(B9), 20111–20122.

Karato, S.-i., Toriumi, M., & Fujii, T. (1980). Dynamic recrystallization of olivine single crystals during high-temperature creep. *Geophysical Research Letters*, *7*(9), 649–652.

Katayama, I., Jung, H., & Karato, S.-i. (2004). New type of olivine fabric from deformation experiments at modest water content and low stress. *Geology*, *32*(12), 1045–1048.

Keefner, J. W., Mackwell, S. J., Kohlstedt, D. L., & Heidelbach, F. (2011). Dependence of dislocation creep of dunite on oxygen fugacity: Implications for viscosity variations in earth's mantle. *Journal of Geophysical Research*, *116*, B05201. https://doi.org/10.1029/2010jb007748

Kohlstedt, D. L., & Hansen, L. N. (2015). *Constitutive equations, rheological behavior, and viscosity of rocks*. Mineral physics (pp. 441–472). Elsevier Inc.

Kohlstedt, D. L., & Ricoult, D. L. (1984). *High-temperature creep of silicate olivines*. Deformation of ceramic materials II (pp. 251–280). Springer.

Kohlstedt, D. L., & Weathers, M. S. (1980). Deformation-induced microstructures, paleopiezometers, and differential stresses in deeply eroded fault zones. *Journal of Geophysical Research*, *85*(B11), 6269–6285.

Lopez-Sanchez, M. A. (2020). Which average, how many grains, and how to estimate robust confidence intervals in unimodal grain size populations. *Journal of Structural Geology*, *135*, 104042.

Lopez-Sanchez, M. A., & Llana-Fúnez, S. (2015). An evaluation of different measures of dynamically recrystallized grain size for paleopiezometry or paleowattometry studies. *Solid Earth*, *6*(2), 475–495.

Mackwell, S. J., Kohlstedt, D. L., & Paterson, M. S. (1985). The role of water in the deformation of olivine single crystals. *Journal of Geophysical Research*, *90*(B13), 11319–11333.

Mainprice, D., Bachmann, F., Hielscher, R., & Schaeben, H. (2015). Descriptive tools for the analysis of texture projects with large datasets using MTEX: Strength, symmetry and components. *Geological Society, London, Special Publications*, *409*(1), 251–271.

Mainprice, D., Hielscher, R., & Schaeben, H. (2011). Calculating anisotropic physical properties from texture data using the MTEX open-source package. *Geological Society, London, Special Publications*, *360*(1), 175–192.

Mei, S., Bai, W., Hiraga, T., & Kohlstedt, D. L. (2002). Influence of melt on the creep behavior of olivine–basalt aggregates under hydrous conditions. *Earth and Planetary Science Letters*, *201*(3–4), 491–507.

Mei, S., & Kohlstedt, D. L. (2000a). Influence of water on plastic deformation of olivine aggregates: 1. Diffusion creep regime. *Journal of Geophysical Research: Solid Earth*, *105*(B9), 21457–21469.

Mei, S., & Kohlstedt, D. L. (2000b). Influence of water on plastic deformation of olivine aggregates: 2. Dislocation creep regime. *Journal of Geophysical Research*, *105*(B9), 21471–21481.

Mercier, J.-C. C., Anderson, D. A., & Carter, N. L. (1977). *Stress in the lithosphere: inferences from steady state flow of rocks*. In Stress in the earth Springer.

Meyers, C. D. (2020). *Laboratory synthesis and experimental deformation of olivine aggregates (Unpublished doctoral dissertation)*. Minneapolis, MN: University of Minnesota.

Montagner, J.-P., & Nataf, H.-C. (1986). A simple method for inverting the azimuthal anisotropy of surface waves. *Journal of Geophysical Research: Solid Earth*, *91*(B1), 511–520.

Morgan, J. W., & Anders, E. (1979). Chemical composition of mars. *Geochimica et Cosmochimica Acta*, *43*(10), 1601–1610.

Morse, S. A. (1979). Kiglapait geochemistry I: Systematics, sampling, and density. *Journal of Petrology*, *20*(3), 555–590.

Park, M., & Jung, H. (2017). Microstructural evolution of the yugu peridotites in the gyeonggi massif, Korea: Implications for olivine fabric transition in mantle shear zones. *Tectonophysics*, *709*, 55–68.

Paterson, M. S. (1982). The determination of hydroxyl by infrared absorption in quartz, silicate glasses and similar materials. *Bulletin de Mineralogie*, *105*(1), 20–29.

Paterson, M. S., & Olgaard, D. L. (2000). Rock deformation tests to large shear strains in torsion. *Journal of Structural Geology*, *22*(9), 1341–1358.

Platt, J. P., & Behr, W. M. (2011). Grainsize evolution in ductile shear zones: Implications for strain localization and the strength of the lithosphere. *Journal of Structural Geology*, *33*(4), 537–550.

Poirier, J.-P. (1985). *Creep of crystals: High-temperature deformation processes in metals, ceramics and minerals*. Cambridge University Press.

Qi, C., Kohlstedt, D. L., Katz, R. F., & Takei, Y. (2015). Experimental test of the viscous anisotropy hypothesis for partially molten rocks. *Proceedings of the National Academy of Sciences*, *112*(41), 12616–12620.

Ranalli, G. (1984). Grain size distribution and flow stress in tectonites. *Journal of Structural Geology*, *6*(4), 443–447.

Ricoult, D. L., & Kohlstedt, D. L. (1985). Experimental evidence for the effect of chemical environment upon the creep rate of olivine. *Point Defects in Minerals*, *31*, 171–184.

Scott, T., & Kohlstedt, D. L. (2006). The effect of large melt fraction on the deformation behavior of peridotite. *Earth and Planetary Science Letters*, *246*(3–4), 177–187.

Skemer, P., & Hansen, L. N. (2016). Inferring upper-mantle flow from seismic anisotropy: An experimental perspective. *Tectonophysics*, *668*, 1–14.

Skemer, P., Katayama, I., Jiang, Z., & Karato, S.-i. (2005). The misorientation index: Development of a new method for calculating the strength of lattice-preferred orientation. *Tectonophysics*, *411*(1), 157–167.

Skemer, P., Sundberg, M., Hirth, G., & Cooper, R. (2011). Torsion experiments on coarse-grained dunite: Implications for microstructural evolution when diffusion creep is suppressed. *Geological Society London Special Publications*, *360*, 211–223. https://doi.org/10.1144/SP360.12

Stipp, M., & Tullis, J. (2003). The recrystallized grain size piezometer for quartz. *Geophysical Research Letters*, *30*(21), 2088.

Stipp, M., Tullis, J., Scherwath, M., & Behrmann, J. H. (2010). A new perspective on paleopiezometry: Dynamically recrystallized grain size distributions indicate mechanism changes. *Geology*, *38*(8), 759–762.

Tasaka, M., Zimmerman, M. E., & Kohlstedt, D. L. (2015). Creep behavior of Fe-bearing olivine under hydrous conditions. *Journal of Geophysical Research: Solid Earth*, *120*(9), 6039–6057.

Tasaka, M., Zimmerman, M. E., & Kohlstedt, D. L. (2016). Evolution of the rheological and microstructural properties of olivine aggregates during dislocation creep under hydrous conditions. *Journal of Geophysical Research: Solid Earth*, *121*(1), 92–113.

Tielke, J.A., Zimmerman, & M.E., Kohlstedt, D.L. (2016) Direct shear of olivine single crystals, *Earth and Planetary Science Letters*, *455*, 140–148. https://doi.org/10.1016/j.epsl.2016.09.002

Tielke, J. A., Zimmerman, M. E., & Kohlstedt, D. L. (2017). Hydrolytic weakening in olivine single crystals. *Journal of Geophysical Research: Solid Earth*, *122*(5), 3465–3479.

Tokle, L., Hirth, G., & Behr, W. M. (2019). Flow laws and fabric transitions in wet quartzite. *Earth and Planetary Science Letters*, *505*, 152–161.

Twiss, R. J. (1977). *Theory and applicability of a recrystallized grain size paleopiezometer*. In Stress in the earth. Springer.

Van der Wal, D., Chopra, P., Drury, M., & Gerald, J. F. (1993). Relationships between dynamically recrystallized grain size and deformation conditions in experimentally deformed olivine rocks. *Geophysical Research Letters*, *20*(14), 1479–1482.

Wallis, D., Hansen, L. N., Tasaka, M., Kumamoto, K. M., Parsons, A. J., Lloyd, G. E., et al. (2019). The impact of water on slip system activity in olivine and the formation of bimodal crystallographic preferred orientations. *Earth and Planetary Science Letters*, *508*, 51–61. https://doi.org/10.1016/j.epsl.2018.12.007

Warren, J. M., & Hirth, G. (2006). Grain size sensitive deformation mechanisms in naturally deformed peridotites. *Earth and Planetary Science Letters*, *248*(1–2), 438–450.

Warren, J. M., Hirth, G., & Kelemen, P. B. (2008). Evolution of olivine lattice preferred orientation during simple shear in the mantle. *Earth and Planetary Science Letters*, *272*(3–4), 501–512.

Withers, A. C., Hirschmann, M. M., & Tenner, T. J. (2011). The effect of Fe on olivine H_2O storage capacity: Consequences for H_2O in the Martian mantle. *American Mineralogist*, *96*(7), 1039–1053.

Woodcock, N. H. (1977). Specification of fabric shapes using an eigenvalue method. *The Geological Society of America Bulletin*, *88*(9), 1231–1236.

Zhang, S., & Karato, S.-i. (1995). Lattice preferred orientation of olivine aggregates deformed in simple shear. *Nature*, *375*, 774–777. https://doi.org/10.1038/375774a0

Zhang, S., Karato, S.-i., Gerald, J. F., Faul, U. H., & Zhou, Y. (2000). Simple shear deformation of olivine aggregates. *Tectonophysics*, *316*(1–2), 133–152.

Zhao, Y.-H., Ginsberg, S. B., & Kohlstedt, D. L. (2004). Solubility of hydrogen in olivine: dependence on temperature and iron content. *Contributions to Mineralogy and Petrology*, *147*(2), 155–161.

Zhao, Y.-H., Zimmerman, M. E., & Kohlstedt, D. L. (2009). Effect of iron content on the creep behavior of olivine: 1. Anhydrous conditions. *Earth and Planetary Science Letters*, *287*(1–2), 229–240.

Zhao, Y.-H., Zimmerman, M. E., & Kohlstedt, D. L. (2018). Effect of iron content on the creep behavior of olivine: 2. Hydrous conditions. *Physics of the Earth and Planetary Interiors*, *278*, 26–33.

Zhong, X., Frehner, M., Kunze, K., & Zappone, A. (2014). A novel EBSD-based finite-element wave propagation model for investigating seismic anisotropy: Application to Finero peridotite, Ivrea-Verbano zone, northern Italy. *Geophysical Research Letters*, *41*(20), 7105–7114.

Zimmerman, M. E., & Kohlstedt, D. L. (2004). Rheological properties of partially molten lherzolite. *Journal of Petrology*, *45*(2), 275–298.